University of California, Merced

Computational Optimization of Concentrating Solar Devices

A dissertation submitted in partial satisfaction of the requirements for the degree Doctor of Philosophy

in

Applied Mathematics

by

Christine Hoffman

Committee:
Professor Boaz Ilan, Chair
Professor Arnold Kim
Professor Sayantani Ghosh

2020

The Dissertation of Christine HOFFMAN, titled "Computational Optimization of Concentrating Solar Devices", is approved, and it is acceptable in quality and form for publication:

Arnold Kim Date

Sayantani Ghosh Date

Boaz Ilan, Chair Date

UNIVERSITY OF CALIFORNIA, MERCED

Abstract

Computational Optimization of Concentrating Solar Devices

by Christine Hoffman

In terms of efficiency, perovskite solar cells have seen the most fastest increase in efficiency. While it took silicon over a decade to reach 20% efficiency, perovskite cells reached similar efficiencies in a matter of years (NREL, 2019), making them the fastest advancing solar technology in history. We will primarily focus on recent advancements in perovskite luminescent solar concentrators (LSCs) with the theoretically optimal values for perovskite LSCs of various compositions and thickness.

The Monte-Carlo simulation framework used to study the effectiveness of luminescent solar concentrators (LSCs) will be established in detail. We use a similar framework to that established by Sahin, Ilan, and Kelley, 2011 for semiconductor nanoparticles. Computational efficiency is improved through implementation of a vectorized Monte Carlo simulation method. Perovskite LSCs are compared against previously used CdSe-CdTe quantum dots. We thereby establish perovskite as a viable, highly efficient LSC as published by Nikolaidou et al., 2016 and obtain ideal perovskite composition and thickness for optimal perovskite LSC performance as published by Mendewala et al., 2019.

The other part of this thesis implements a deterministic ray tracing algorithm combined with appropriate optimization methods to evaluate the performance of segmented non-imaging solar thermal concentrators. Under user-specified parameters and constraints, new concentrator configurations are obtained which optimize theoretical efficiency. Such configurations have not yet been discussed in literature.

Pattern search, a gradient free optimization method, is employed to determine ideal segment positions. The presence of numerous local minima make gradient-based optimization solvers ineffective.

Acknowledgements

I would like to thank my advisor, Professor Boaz Ilan, for his continuous support and patient explanations. Thank you for sharing a part of your vast knowledge with me. And most importantly, thank you for your incredible kindheartedness on this journey. Research has it's ups and down, but despite the situation, thank you for your encouragement, smile, and constant offer of a cup of tea.

And finally, I also want to thank my husband, Rafay Qureshi. Thank you for always being there for me and never letting me give up.

Christine Hoffman

choffman7@ucmerced.edu

EDUCATION

University of California, Merced — GPA: 3.74
PhD in Applied Mathematics — **August 2020**

University of California, Merced — GPA: 3.74
Master of Science in Applied Mathematics — **May 2017**

Smith College, Northampton, Massachusetts — GPA: 3.90
Post-Baccalaureate Certificate in Mathematics — **May 2014**

University of Minnesota, Morris — GPA: 3.85
Bachelor of Arts in Mathematics and Spanish, minor: Chemistry — **May 2013**

RESEARCH

Graduate Research, principle investigator: Boaz Ilan — 2014 –2020
Mathematical Modeling of Light Propagation in Solar Energy Devices

Graduate-level Research in Industrial Projects in Sendai, Japan — June –August 2019
FUJITSU Laboratories Ltd.: Resolving real-world issues by "Digital Annealer"

Laurence Livermore National Lab Data Science Challenge — May 2019
Intense data science training program using reinforcement learning, PI: Brenden Petersen

DAAD Rise Professional, Helmholtz-Zentrum Berlin for Materials and Energy — May –August 2017
Spectroscopic Characterization of Energy-Conversion Devices, PI: Marcus Bär

NASA Summer Internship, Goddard Space Flight Center — June –August 2016
Radiative Transfer Calculations for Remote Sensing of Greenhouse Gases, PI: Emily Wilson

Smith Graduate Student Research, PI: Joseph O'Rourke & Christophe Golé — 2013 –2014
Convex Surface Hulls of Two Circles in Space & Self-Similarity of Snail Shells

Cornell University Summer Math Institute, PI: Ravi Ramakrishna — June –August 2013
Program in algebra coursework and research on aperiodic tilings of the plane

Applied Mathematics REU, **University of Nebraska Lincoln** — June –July 2012
Peridynamics Models in Heat Conduction and Elasticity, principle investigator: Petronela Radu

Senior Paper in Number Theory, principle investigator: David Roberts — 2011 –2012
Maximal Subgroup Elimination Applied to Galois Theory

PUBLICATIONS

B. Mendewala, K. Nikolaidou, **C. Hoffman**, S. Sarang, J. Lu, B. Ilan, S. Ghosh: The potential of scalability in high efficiency hybrid perovskite thin film luminescent solar concentrators, *Solar Energy*, 183:392-397, 2019.

B. Ilan, **C. Hoffman**, and C. Rimland: Computational optimization for nonimaging solar concentrators using generalized pattern search *Nonimaging Optics: Efficient Design for Illumination and Solar Concentrators XV*, (Vol. 10758, p. 107580L). International Society for Optics and Photonics (SPIE) 2018

E. Wilson, A. DiGregorio, V. Riot, M. Ammons, W. Bruner, D. Carter, J. Mao, A. Ramanathan, S. Strahan, L. Oman, **C. Hoffman**, R. Garner: *A 4U laser heterodyne radiometer for methane (CH_4) and carbon dioxide (CO_2) measurements from an occultation-viewing CubeSat*,
Measurement Science and Technology, Vol. 28, No. 3, 2017.

K. Nikolaidou, S. Sarang, **C. Hoffman**, B. Mendewala, H. Ishihara, J. Q. Lu, B. Ilan, V. Tung, and S. Ghosh: *Hybrid perovskite thin films as high-efficiency luminescent solar concentrators*, Advanced Optical Materials 2016.

AWARDS, FELLOWSHIPS, AND SCHOLARSHIPS

2020 Graduate Dean's Dissertation Fellowship
2017 –2018 Graduate Student Researcher
2017 GradSLAM Campus Runner-Up
2016 John Mather Nobel Scholar Award
2016 –2017 Faculty Mentor Program Fellowship
2015 –2017 Dan David Solar Fellowship
2016 OSA Best Student Paper Award
2012 –2013 Bos Undergraduate Research Award
2012 –2013 Karyn Nielson Memorial Scholarship
2012 –2013 Phi Mu Delta Scholarship
2010 –2013 Morris Scholar
2010 –2013 Gertrude Gaffney Hanlon Scholarship

PRESENTATIONS

Modeling and Optimization: Theory and Applications, Lehigh University August 2019
Presentation on *Computational Optimization for Nonimaging Solar Concentrators using Generalized Pattern Search*

Optics and Photonics for Energy & the Environment, OSA November 2017
Presentation on *Mini-Laser Heterodyne Radiometer for CO_2 and CH_4 Measurements*

Optics for Solar Energy, OSA Light, Energy and the Environment Congress November 2016
Presentation on *Hybrid perovskite thin films as high-efficiency luminescent solar concentrators*

National Labs Day, University of California-Merced October 2016
Poster Presentation on "Mini-Laser Heterodyne Radiometer for CO_2 and CH_4 Measurements"

Hudson River Mathematics Conference, Marist College April 2014
Presentation on *Self-Similarity of Snail Shells*

AMS Special Session on Research in Mathematics, Joint Mathematical Meetings January 2014
Presentation on *Developing Surfaces that are Hulls of Two Circles in Space*

Women In Mathematics In New England Conference, Smith College September 2013
Research talk on "On the Spectrum of the Penrose Laplacian"

AMS Session on Undergraduate Research in Analysis, Joint Mathematical Meetings January 2013
Presentation on *Nonlocal Models in Diffusion with Applications in Peridynamics*

Senior Thesis Presentation, University of Minnesota-Morris April 2012
Presentation on "Finding Galois Groups Through Maximal Subgroup Elimination"

TEACHING EXPERIENCE

Teaching Assistant, University of California, Merced August 2014 –December 2019

CalTeach Spring Externship, NatureBridge & UC Merced March 2018

Mathematics Teacher, HS^2 Program, Colorado Rocky Mountain School June –July 2015

Instructional Intern, Center for Engaged Teaching and Learning 2014 –2015

Teaching Intern, Summer Session, Northfield Mount Hermon School June –August 2014

Teaching Assistant and Tutor of Mathematics, Smith College 2013 –2014

Volunteer Math & Science Tutor, Project Coach 2013 –2014

Urban Education Volunteer Teaching Fellow, Renaissance School, Springfield, MA March 2014

Tutor of Mathematics, Chemistry, & German, University of Minnesota, Morris 2010 – 2012

CONFERENCES AND WORKSHOPS

Modeling and Optimization: Theory and Application (MOTA) August 2019

Optical Society of America Light, Energy and the Environment Congress November 2017

Optical Society of America Light, Energy and the Environment Congress November 2016

Advanced Computing for Earth Sciences May –June 2016

Solar Research Symposium October 2015

Hudson River Mathematics Conference April 2014

Joint Mathematical Meetings 2014 January 2014

Women In Mathematics In New England September 2013

Joint Mathematical Meetings 2013 January 2013

Women in Mathematics 2012 May 2012

COMPUTER SKILLS

Matlab **Mathematica** **Python** **LaTex** / **Beamer**

PROFESSIONAL AFFILIATIONS

AAAS, American Association for the Advancement of Science

SIAM, Society for Industrial and Applied Mathematics

OSA, Optical Society of America

LANGUAGE SKILLS

German: Fluent in Reading, Writing, & Conversation

Spanish: Highly Advanced in Reading, Writing, & Conversation

Hindi/Urdu: Advanced Reading & Conversational Skills, basic Urdu writing

EDUCATIONAL EXPERIENCES ABROAD

U.S. Department of State Urdu Critical Language Scholarship Summer 2018
American Institute of Indian Studies, Lucknow, India (Credit: Bryn Mawr College) GPA: 3.43

National Student Exchange Fall Semester 2012
InterAmerican University of Puerto Rico, San Germán GPA: 4.00

South Korea University 2012 Spring Break Scholarship March 2012
Yonsei University, Korea Foundation and CIEE

Summer Renewable Energy Internship, Genesis Project, Jülich, Germany May –August 2011

Congress Bundestag Youth Exchange Scholarship to Germany, U.S. Department of State 2008 –2009

Contents

List of Figures

List of Tables

Part I

Nonimaging Solar Thermal Concentrators

Chapter 1

Introduction

Renewable energy sources, such as solar, have seen rapid increases in recent years as greenhouse gas reduction initiatives become more prevalent worldwide. Renewable energy production has more than doubled between 2001 and 2018, with solar energy experiencing a thirteen fold increase over this same period (Administration, 2019). Increases in solar efficiency and decreasing costs have contributed to the impressive rise in solar energy production.

With rising levels of greenhouse gas emissions and pollution globally, many countries are pushing towards expanding renewable energy. Solar energy alternatives have recently seen a soar in popularity due to their lower environmental impact, recent plummets in costs, and enhanced grid stability when compared with fossil fuel sources.

In recent years, renewable energy electricity costs have been comparable, or cheaper, than fossil-based energy as solar PV costs decreased by 83% between 2010 and 2017 (IRENA, 2018). The decrease in costs are a result of increases in efficiency and decreasing manufacturing costs.

Some renewable energy sources, especially solar, specifically lend themselves to localized energy production. Local energy production has many advantages over centralized energy generation. In 2019, 25,281 power outages effected 28.4 million people, a 50% increase from the 19 million affected in 2018 [1].

A portion of these power outages were due to wildfire prevention measures. Some power lines pass through windy, dry regions between the electricity plant and customer homes. Power was preemptively turned off during times of high wildfire risk. In this way, centralized energy generation can be more more vulnerable to power outages when any link from the power plant to the customer is out of service. In addition, power outages from centralized sources put entire regions without power, instead of a single individual home.

Solar energy can eliminate or reduce energy transmission distance, hence eliminating outages caused by downed power lines. Localized rooftop solar enhance grid stability by reducing large regional outages. Rooftop solar installations also reduce the amount of land usage. Centralized power include a large power plant and extending power lines, both of which require land resources.

[1] BloomEnergy California Power Outage Map `https://www.bloomenergy.com/bloom-energy-outage-map`

Some of the drawbacks of the decentralized nature of rooftop solar are maintenance and repair costs that often fall on individual home and business owners instead of the power company. In addition, the fragmented power supply system proves to be much more complicated for power companies to regulate. Ideally there should always be enough power generated to satisfy demand without producing a large oversupply of power that goes unused.

1.1 Main Types of Solar Energy

There are two main types of solar energy devices. The first, known as photovoltaics, or PVs, convert the energy from the sun directly into electricity through the photoelectric effect. The second, known as solar thermal, captures radiation from the sun in the form of heat. While electricity from PV solar devices can be converted into heat, efficiency losses from the conversion of solar radiation into electricity and then into heat makes process much less efficient than directly using solar radiation as heat. Similarly, solar thermal energy can be converted into electricity through the use of turbines.

PV solar cells are generally flat panels, as shown in Figure 1.1, whereas solar thermal thermal technology typically has pipes to transport collected thermal heat to a heat exchanger and storage tank. Concentrating back mirrors curve around the receiving pipe, as shown in Figure 1.2.

FIGURE 1.1: Flat rooftop PV solar panels

1.1.1 Advantages and Disadvantages of PV and Solar Thermal

PV solar is the most effective for localized electricity needs. Conversion of solar thermal to electricity requires the installation of steam powered turbines powered whose size and expense are only practical at the industrial level. Rooftop PV can provide electricity at lower costs than that from fossil fuel sources. Consumers can even earn credits for electricity

FIGURE 1.2: Solar thermal Compound Parabolic Concentrator

sold back to the grid when household electricity supply exceeds demand. However, the high upfront cost of PV solar panel costs and installation is one of the largest deterrents.

In general rooftop PV systems require very little maintenance. However, when maintenance is required, it is often the homeowners responsibility. Homeowners carry the burden of installation and upkeep of any localized rooftop system, versus relying on power companies for generation and maintenance. Localized power generation provides some degree of independence from outside power suppliers, depending on the amount of energy generated and local storage capacity. Hence, localized systems are unaffected by centralized system power outages.

Despite local system energy generation independence, most homeowners are not able to go completely “off grid" due to the inability to generate and store enough electricity to meet household demands all day and year round. PV solar cell electricity output is highly variable, depending on the amount of sunlight received. Solar PV is considered a variable renewable energy since electricity output dips considerably even when the sun moves behind a cloud and immediately drops to zero when the sun sets.

Solar thermal, on the other hand, is better able to deal with solar fluctuations due to its more natural built-in storage capacity. Unlike PV solar, which requires large battery packs to store energy, solar thermal can store energy in the form of heat in insulated vessels. This leads to more consistent energy output from solar thermal devices than solar PV.

In general, it is important to note that solar PV and solar thermal compliment, instead of replace, one another. Solar PV is best able to provide household electricity needs. Compared to the solar PV array size needed to reach household electricity requirements, a more compact solar thermal system can satisfy household hot water heating demands. Although solar thermal systems can be used for cooling, this requires the installation of an additional evaporative cooling systems, which adds to cost, space, and maintenance.

	Advantages	Disadvantages
Photovoltaics	low electricity cost	high upfront costs
	low maintenance costs	homeowner maintained
	reliable localized energy	inconsistent electricity output
	high electricity efficiency	high storage costs
Solar Thermal	consistent energy output	higher maintenance costs
	reliable localized energy	bulkier devices
	lower-cost storage	storage space required
	efficient heat/cooling	electrical conversion losses

TABLE 1.1: The above table shows the advantages and disadvantages of solar thermal versus solar electric.

Solar Energy Storage

Photovoltaic solar panels, the most common form of solar energy, are only able to produce energy during daylight hours and their energy output in megawatts with respect to time of day is shown in grey in Figure 1.3. However, the total energy demand, shown in blue, peaks in the evening around 8pm, often after the sun has set. This offset in renewable photovoltaic solar energy availability and energy demand creates what is known as the "duck curve", shown in orange. The "duck curve" is the shape of the graph created by subtracting the solar energy supply from the energy demand curve.

The most notable problematic feature of this graph is the steepness of the graph around 5-7 pm. The evening decrease in solar photovoltaic energy that aligns with the peak time of energy consumption usage creates a sudden increase in demand for another energy source, often from nonrenewable sources. Storing solar photovoltaic energy requires the usage of expensive battery storage, a major pitfall for maintaining affordable renewable electricity during nighttime hours.

Energy storage capability is one advantage of solar thermal energy over solar photovoltaics. Solar thermal energy is naturally stored more cost effectively in the form of heat in thermally insulated vessels. While solar thermal energy is still only produced during daylight hours, it naturally lends itself to easier storage, particularly for short periods of time.

Cost-effective short term energy storage creates the opportunity for solar thermal energy to be used up to a few hours after sunset, when energy demand is the highest. Natural low-cost thermal energy storage provides more consistent and flexible energy even during daylight hours when PV systems might otherwise show a dip energy output.

The energy capacity of concentrating solar power has increased by ten times worldwide between 2006 and 2016 (IRENA, 2018). The costs of concentrating systems will further decrease as the number of installations expands.

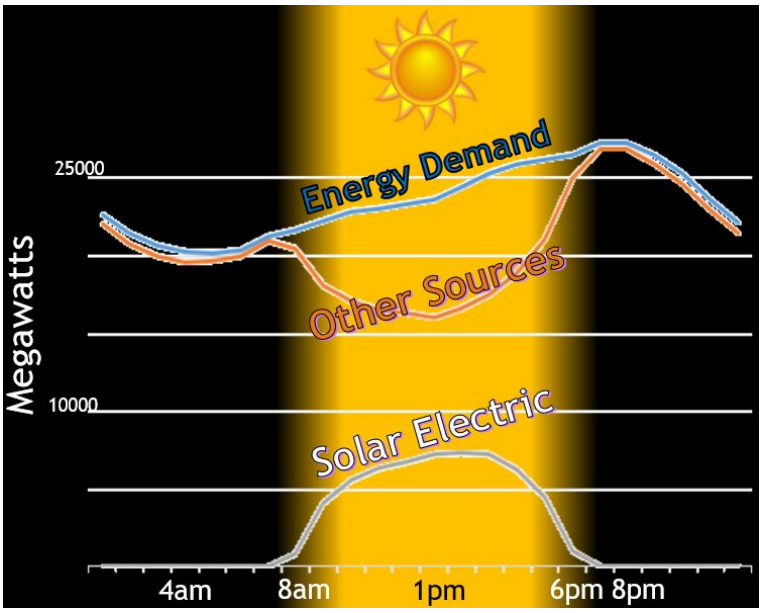

FIGURE 1.3: The following image shows the effect of wind and photovoltaic solar on the energy demand. Image adapted from Reinhold, 2016.

1.2 Solar Thermal Concentrators

This part of the thesis will focus exclusively on solar thermal concentrators. The rest of this chapter will specifically describe the design and setup of nonimaging concentrators, along with their uses and recent advancements.

The following chapter will describe the ray tracing setup used to evaluate the performance of various nonimaging solar thermal concentrator configurations, along with the optimization procedure used for certain designs to obtain more ideal configurations for higher power output. When installed, manufacturing and setup procedures introduce inherent flaws, which we quantify using uncertainty quantification. We then summarize our work and describe future research directions.

1.2.1 Main Categories of Solar Thermal Concentrators

There are two categories of concentrators: imaging and nonimaging. As the name suggests, imaging concentrators form an image of the source onto the receiver, whereas nonimaging concentrators do not.

Imaging optics produce clearly defined images of the source onto the receiver, as shown in Figure 1.4. Rays do not cross and rays originating from the same point on the source land at the same point on the receiver to produce that image. Imaging concentrators are

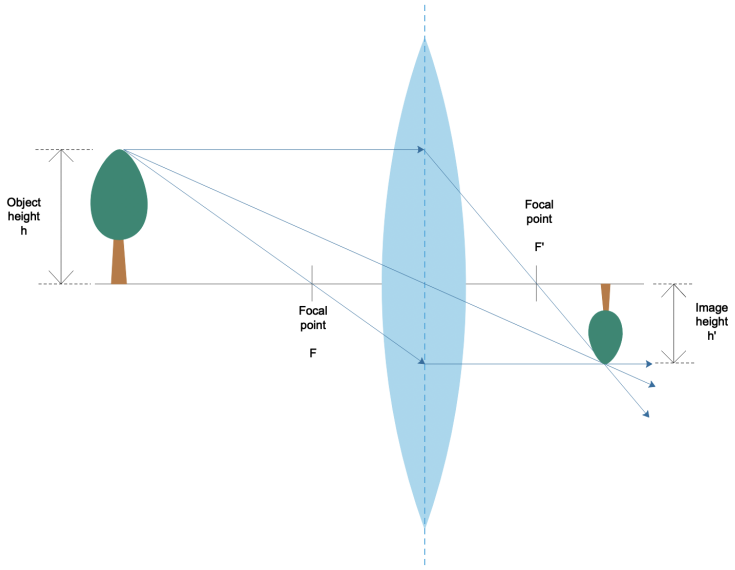

FIGURE 1.4: An imaging optic is shown which produces an image of the source onto the receiver.

currently used in existing large scale solar thermal systems due to their high concentration ratios, which range from tens to the mid hundreds.

Nonimaging concentrators have comparatively much lower concentration ratios, generally below 10 (Duffie and Beckman, 2013). Nonimaging solar concentrators rose in prominence in the 1960's with the discovery of compound parabolic concentrators (CPC) (Koshel, 2012).

Nonimaging optics do not necessarily form images of the sources, meaning that rays originating from the same point on the source may not end up at the same location on the receiver, as shown in Figure 1.5. Furthermore, rays may cross, as shown by the orange rays which originate from the same point on the source but cross paths before striking the receiver.

Tracking VS Non-Tracking

In terms of concentration, the main difference in imaging versus nonimaging is the acceptance angle. Imaging requires tracking. Nonimaging concentrators allow a wide acceptance angle without tracking or only partial season tracking. The non-tracking advantage of nonimaging concentrators means there are fewer moving parts, and hence less maintenance required of nonimaging concentrators. Imaging concentrators require a tracking device to maintain their concentration ratios, which adds to the maintenance and cost of such devices.

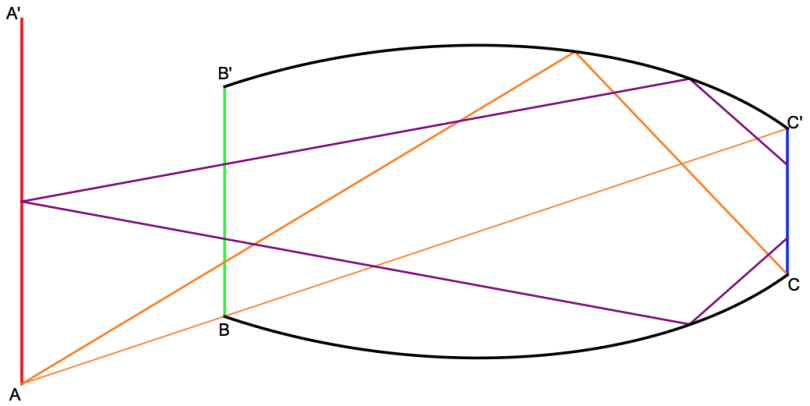

FIGURE 1.5: A nonimaging optic is shown. Since an image in not necessarily formed of the source on the receiver, rays originating from the same point on the source may land at different location on the receiver and may even cross, as shown by the purple and orange rays originating from distinct points on the source.

Nonimaging concentrators are able to reflect incident radiation onto the aperture over a range of incident angles. This wide limit is known as the **acceptance angle** of the concentrator. Collecting all incident radiation within the acceptance angle means diffuse radiation is also absorbed (Duffie and Beckman, 2013). Therefore, 100% of radiation within the acceptance angle falls incident onto the receiver.

Temperature Differences

Nonimaging solar concentrators fill the temperature gap between flat plate absorbers and large scale high temperature concentrating facilities. As shown in Figure 1.6, nonimaging solar concentrators such as the Artic Solar XCPC achieve temperatures within the range of approximately $100°C - 200°C$. Such temperatures are ideal for use in industrial hot water, industrial drying, desalination, and evaporative cooling.

1.2.2 Background on Nonimaging Solar Concentrators

Nonimaging solar concentrators have the advantage of being non-tracking solar devices, meaning that no moving mechanical device is needed. As their name suggests, nonimaging concentrators do not necessarily form an optical image of the source, but rather instead aim to maximize all forms of solar light radiation, beam or diffuse, onto the receiver (Duffie and Beckman, 2013). Of the earliest work on nonimaging optics, the most developed framework was presented by Hinterberger and Winston, 1966.

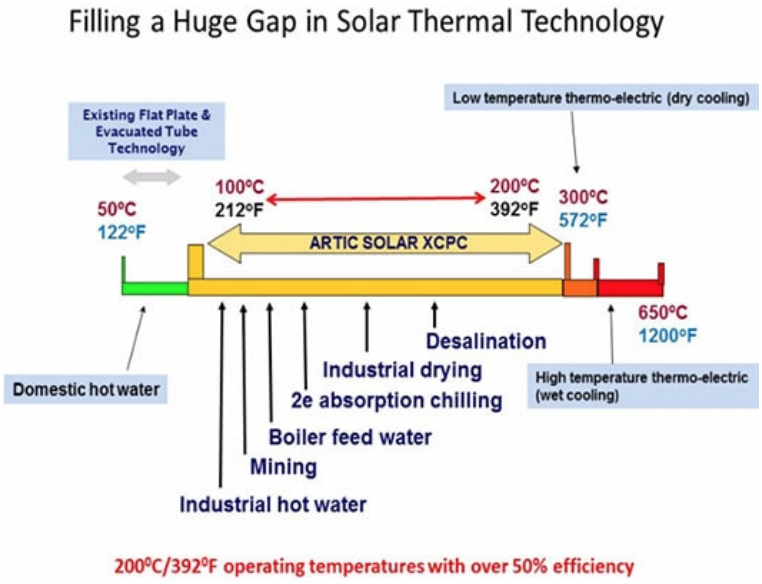

FIGURE 1.6: Nonimaging concentrators fill the temperature range gap between flat plat absorbers and high temperature concentrating facilities. Diagram from Artic Solar (http://www.articsolar.com/).

Solar thermal concentrators have the natural ability to store the sun's energy as heat, which can even be used several hours after the sun sets. In addition, solar thermal concentrators naturally compliment solar electric systems in their ability to efficiently cool and heat. Heating and cooling processes are generally electricity intensive and can quickly exhaust solar electric outputs. Nonimaging solar thermal concentrators have been utilized as a heating system during colder months and as cooling systems using evaporative cooling techniques during warmer months. Standard heating and cooling systems require large amounts of electricity and are largely powered using fossil fuels, such as natural gas.

1.2.3 Concentration Ratio

A solar thermal concentrator is an optical device between a radiation source and a receiver which causes more rays of sunlight to strike the receiver than if the receiver were to face the sun and collect rays without the concentrating optical device. In other words, a concentrator increases energy density by decreasing receiver area from which heat losses occur but retaining the same energy delivery as a flat-plate receiver of equivalent aperture area, thereby increasing the concentration ratio.

The concentration ratio is a benchmark used to assess the effectiveness of a solar thermal concentrator. A higher concentration ratio would correlate to a better concentrating optic. Better concentrating optics direct higher amounts of additional energy onto the receiver,

resulting in higher energy density increases compared to what the receiver would otherwise receive without the optic. The two concentration ratios used commonly used to compare solar thermal concentrators are the geometrical and optical concentration ratios.

Geometric Concetration Ratio

The **geometric concentration ratio** is defined as the ratio of the area of the aperture to the area of the receiver, written as,

$$C_{geometrical} = \frac{A_a}{A_r} \tag{1.1}$$

where A_a is the area of the aperture, and A_r is the area of the receiver.

The **receiver** is the element where the radiation is absorbed and the **aperture** is the opening through which the solar radiation enters the concentrator. The **concentrator** is the optical system compoenent of the collector that directs radiation onto the receiver and the **collector** is the term used for the complete system, which includes the aperture, receiver, and concentrator (Duffie and Beckman, 2013). In this paper, the sun will be referred to as the energy source, or simply **source**.

The maximum concentration ratio derived in Rabl, 1976 is based on the second law of thermodynamics applied to the radiative heat exchange between the source and the receiver, both of which are assumed to be a perfect blackbody. The Stephan-Boltzman law states that the radiation power density from a perfect blackbody source onto any point at distance R from the source will be,

$$P_s = \frac{r^2}{R^2}\sigma T_s^4 \tag{1.2}$$

where $\sigma = 5.67\times10^{-8} W m^{-2} K^{-4}$ is the Stefan Boltzmann constant, T_s is the equilibrium temperature of the source, r is the radius of the source as viewed from the point at distance R and P_s is the power density of the source at a point of distance R from the source. The concentrator setup is shown in Figure 1.7.

The total power radiated from the source onto the aperture is then given by,

$$P_{s\to a} = A_a \frac{r^2}{R^2}\sigma T_s^4 \tag{1.3}$$

where A_a is the area of the aperture which in this case is at distance R from the source, and $P_{s\to a}$ is the total power from the source onto the aperture. We are interested in the maximum concentration ratio, meaning that of an ideal concentrator in which the total power received at the aperture is also that received at the receiver. Hence,

$$P_{s\to r} = A_a \frac{r^2}{R^2}\sigma T_s^4 \tag{1.4}$$

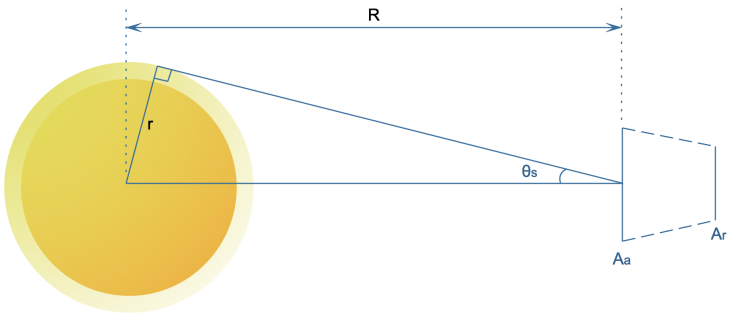

FIGURE 1.7: Sketch of the source of radius r radiating towards a concentrator at a distance of R with aperture area A_a and receiver area of A_r. θ_s is the half angle subtended by the source.

where $P_{s\to r}$ is the total power from the source onto the receiver.

Assuming the receiver is also a perfect blackbody, the total power radiated from the receiver is,

$$P_r = A_r \sigma T_r^4 \tag{1.5}$$

where A_r is the area of the receiver and T_r is the equilibrium temperature of the receiver. Only a fraction of the power from the receiver to the source, $F_{r\to s}$, reaches the source, meaning,

$$P_{r\to s} = A_r \sigma T_r^4 F_{r\to s} \tag{1.6}$$

where $P_{r\to s}$ is the total power from the receiver to the source. When $T_r = T_s$, the second law of thermodynamics states that $P_{s\to r} = P_{r\to s}$. Therefore, combining equations (1.4) and (1.6) yields the following ratio:

$$\frac{A_a}{A_r} = \frac{R^2}{r^2} F_{r\to s} \tag{1.7}$$

Since the $\max F_{r\to s} = 1$, the maximum concentration ratio of equation (1.1) for linear two dimensional concentrators is

$$\max[C_{geometrical}] = \max\left[\frac{A_a}{A_r}\right] = \frac{1}{\sin(\theta_s)} \tag{1.8}$$

where θ_s is the half angle subtended by the source as shown in Figure 1.7. Note that the while the geometric concentration ratio can have any value, the value of the geometrical concentration limit is only meaningful when all of the light incident on the collector aperture within the prescribed acceptance angle reaches the receiver without any loss (O'Gallagher, 2008). Applying the approximate half angle subtended by the sun from earth of $\theta_s = 0.27°$,

the maximum possible concentration ratio for linear two-dimensional concentrators is 212 (Duffie and Beckman, 2013).

Optical Concetration Ratio

Note that equation (1.8) refers purely to the geometric concentration ratio and is used to derive the maximum possible concentration ratio, whether physically possible or not. A more accurate measure of the performance of an actual concentrator is the **optical concentration ratio**. The optical concentration ratio is the portion of incident rays on the aperture within a specified collecting angle that reach the receiver. The optical concentration ratio will always be less than or equal to the theoretical maximum geometric concentration ratio (Winston et al., 2005).

The optical concentration ratio is determined by integrating the averaged irradiance, or radiance flux I_r, over the receiver area, A_r, and dividing this quantity over the solar irradiance incident on the collector aperture, I_a. (Stine and Geyer, 2001).

$$C_{optical} = \frac{\frac{I}{A_r}\int I_r dA_r}{I_a} \tag{1.9}$$

Optical efficiency can also be determined by tracing rays through a concentrator system to find the proportion of incident rays on the aperture within a given collecting angle that reach the receiver. In this paper, we will primarily use the optical concentration ratio as a measure for the effectiveness of a particular concentrator configuration.

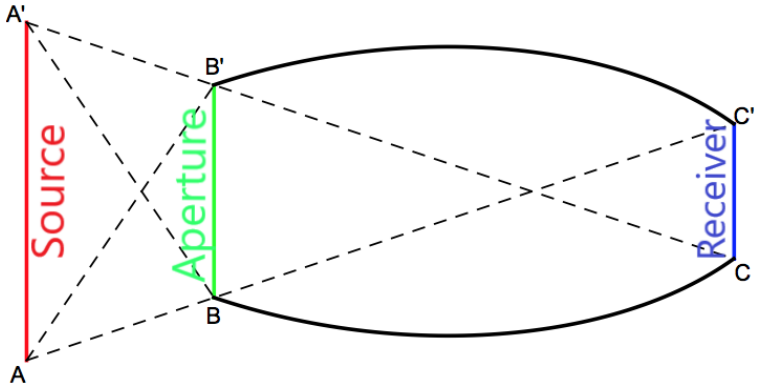

FIGURE 1.8: Diagram showing how the method of strings and edge ray principle are used to design ideal 2D nonimaging solar thermal concentrators.

1.2.4 Compound Elliptical Concentrators (CECs)

Ideal two dimensional solar thermal concentrators are designed using the method of strings, which utilizes principles from Hottel's strings and the edge ray principle. Hottel's strings

were originally used to calculate radiation transfer between walls in a furnace (Winston, Jiang, and Ricketts, 2018). The edge ray principle, based on Hamiltonian and Lagrangian optics, states that redirecting all light rays emanating from the edges of the source towards the edges of the receiver will ensure that all the light rays from the interior of the source will also land on the receiver.

An example of an ideal 2D compound elliptical concentrator (CEC) setup is shown in Figure 1.8. The linear source, shown on the left in red, and linear receiver, show on the right in blue, must first be defined. A CEC is uniquely defined for any given extended linear source and linear receiver. Every point on the source is assumed to radiate isotropically. Cross strings $\overline{AC'}$ and $\overline{A'C}$ are drawn from the bottom of the source to the top of the receiver and from the top of the source to the bottom of the receiver, respectively.

A concentrator is only considered ideal when every ray emanating from the source that enters the aperture also eventually hits the receiver. Hence the solid black concentrator arms must be designed such that all rays emanating from the source $\overline{AA'}$ and crossing $\overline{BB'}$ must be reflected by the concentrator onto $\overline{CC'}$. One way to design such a concentrator is to use the cross strings to draw upper and lower concentrator arms based on what is known as the edge ray principle (Winston, Jiang, and Ricketts, 2018).

The edge ray principle directs rays originating from the most extreme points on the source, such as those at A and A' onto the most extreme points on the receiver, C and C' respectively. A unique ellipse can be defined by denoting two unique foci points A and C and a point on the ellipse, C'. A portion of such an ellipse uniquely determines the solid black top concentrator portion in Figure 1.8.

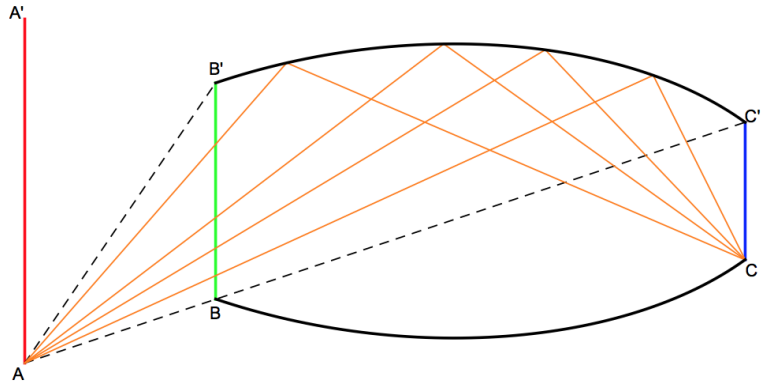

FIGURE 1.9: Source edge rays generated from one focus, shown in orange, hitting the elliptical concentrator will be directed towards the edge of the receiver corresponding to the opposite focal point of the ellipse.

By the properties of an ellipse, all rays generated from focus point A that cross the aperture will hit the upper elliptical concentrator and be reflected to the opposite focus at point C. All rays traveling within the cone between $\overline{AB'}$ to $\overline{AB}$ will be reflected to point C on the receiver, as shown in Figure 1.9. Note that the rays $\overrightarrow{AB'}$ and $\overrightarrow{AB}$ hit the very edges

of the concentrator on either side of the aperture. Determining whether such rays hitting the exact edges of the aperture enter the aperture or not is impossible. Hence, such cases are removed and assumed not to enter the aperture in ray tracing simulations mentioned later in this paper.

Similarly, all rays generated from point A' that cross the aperture will hit the lower elliptical concentrator and be reflected to the opposite focus at point C'. This is due to the fact that A' is one focal point of the ellipse and C' is the other of the bottom elliptical concentrator. Only rays within the cone between $\overline{A'B}$ to $\overline{A'B'}$ are reflected towards C'. Rays at the exact extreme edges of this cone, namely rays $\overrightarrow{A'B}$ to $\overrightarrow{A'B'}$, are not considered to enter the aperture in ray tracing simulations.

Given that all rays generated on either edge of the source which enter the aperture are concentrated onto the receiver, an argument of continuity implies that all rays generated from the interior of the source that cross the aperture must also be concentrated onto the receiver. Hence all rays from the source entering the aperture are concentrated onto the receiver. Such concentrators are considered ideal since such designs can reach the thermodynamic concentration ratio limit (Winston, Jiang, and Ricketts, 2018).

Note that the acceptance angle for a CEC is not fixed, but rather depends on the location on the aperture. For example, any point D located on the aperture $\overline{BB'}$ in Figure 1.8 would accept rays traveling within the cone $\overline{AD}$ to $\overline{A'D}$. Given the acceptance angle ray dependence on the location where it crosses the aperture, there is not a sharp cutoff in incident radiation collected for a specific ray theta value at the aperture.

1.2.5 Asymmetric Nonimaging Concentrators

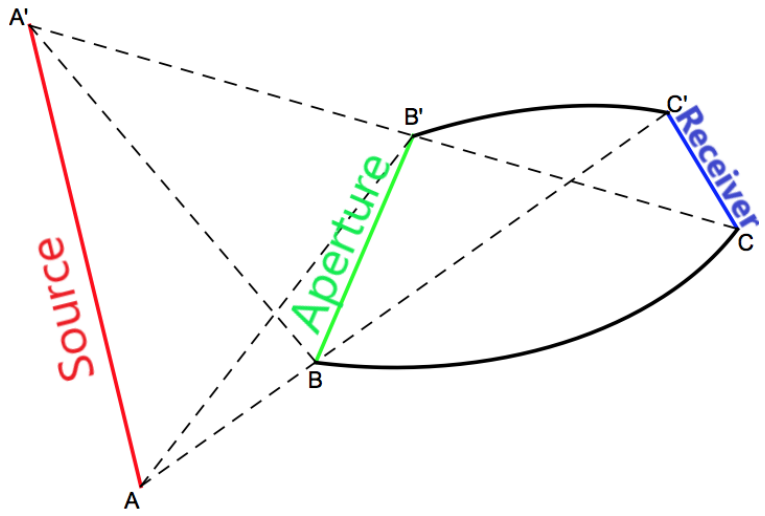

FIGURE 1.10: Asymmetry arises when the receiver is chosen not be parallel with the source.

When the uniquely defined source and the receiver for a CEC are not parallel, the resulting concentrator shape will not be symmetric, as shown in Figure 1.10. Such collectors are known as asymmetric nonimaging concentrators.

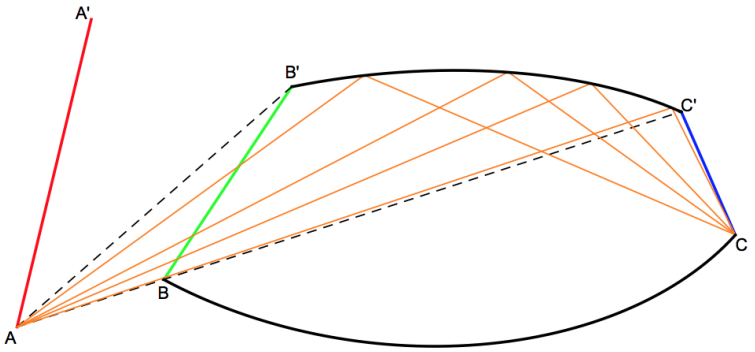

FIGURE 1.11: The cone of source edge rays generated, shown in orange, is different at each end of the source.

1.2.6 Compound Parabolic Concentrators (CPCs)

Compound parabolic concentrators can be thought of as an extension of CECs with the source at infinity, filling the entire plane. Consider any CEC with elliptical concentrator,

$$\frac{x^2}{a^2} + \frac{y^2}{b^2} = 1 \qquad \text{and eccentricity} \qquad \sqrt{1 - \left(\frac{b}{a}\right)^2}$$

where a is the semi-major axis and b is the semi-minor axis. As the source goes to infinity, the semi-major is extended until the eccentricity equals,

$$\lim_{a \to \infty} \sqrt{1 - \left(\frac{b}{a}\right)^2} = 1$$

Each side of the concentrator is now a parabola, since the conic section with eccentricity equal to 1 is a parabola. However, since the source at infinity is now a plane, using the previous method of concentrator design will result in a planar concentrator. In other words, the concentrator and the receiver will be the same, resulting in simply a flat plate absorber.

Radiation from only a section of the sky within a specified acceptance angle will be concentrated onto the receiver. A CPC is uniquely defined given a linear receiver and a specified acceptance angle

1.2.7 Limitation of String Method Concentrators

The method described to design solar concentrators by the string method results in continuously varying shapes. Such designs are not easy to manufacture since they require precise

continuous bending of a highly reflective material. Furthermore, the approach is limited to 2D designs. While the design can be extended to three dimensions through either a trough design symmetric about and axis or through a rotationally symmetric design that produces what is known as Winston cones. Neither of these extensions is ideal in 3D, despite being based off of the ideal 2D design. By not ideal in 3D, it is meant that not all rays that enter the aperture are collected on the receiver. This is mainly due to skew rays that enter at angles which do not lie in a plane that includes through the central axis of the CPC.

1.2.8 Current Design and Manufacturing Production

Current production of nonimaging solar thermal concentrators includes precise bending of a reflective material, typically metal sheets. The sheet must not only bend, but also retain the ideal compound parabolic concentrator (CPC) trough configuration. To achieve this, continuous bending along with heat are required in trough production. Initial upfront costs are seen as one of the largest barriers to solar energy installations (Concerned Scientists, 2017).

One manufacturer, Artic Solar, has turned to segmented nonimaging solar thermal concentrator trough designs such as those shown in Figure 1.12. Segmented nonimaging solar thermal concentrator designs differ from the smooth ideal CPC design in that the troughs are not a smooth curved surface, but rather consist of flat surfaces joined at the edges. Such designs are also known as faceted concentrators. In this way, concentrators may be produced from a single flat reflective piece of metal that is kinked at the various joints to the desired angle between adjacent flat segments.

Reflective metal sheets are better able to retain their shape when kinked at joints to form hinges of a desired angle rather than bent continuously into a smooth curve. Hence concentrators made by hinging flat sheets may be produced more cheaply without significant added heat or continuous bending. Hence manufacturing cost reduction is the driving motivation for the segmented nonimaging solar concentrator designs discussed in this paper.

Despite the possible reduction in manufacturing costs, alternative designs to the ideal nonimaging 2D compound parabolic concentrator (CPC) trough design also face a drawback; they are less than ideal, meaning less than ideal configurations do suffer from some efficiency loss. The reduction in manufacturing costs may outweigh the reduction in efficiency since some companies, such as Artic Solar, are already choosing to manufacture segmented nonimaging solar thermal concentrators rather than the traditional smooth CPC design.

Current designs place segmented solar thermal concentrator joints at locations from a discrete subset of points of the ideal CPC without optimization. The goal of this paper is to compare the efficiency of segmented solar thermal concentrators with optimally placed joints versus segmented solar concentrators with an equivalent number of joints placed at discrete locations from the ideal CPC configuration.

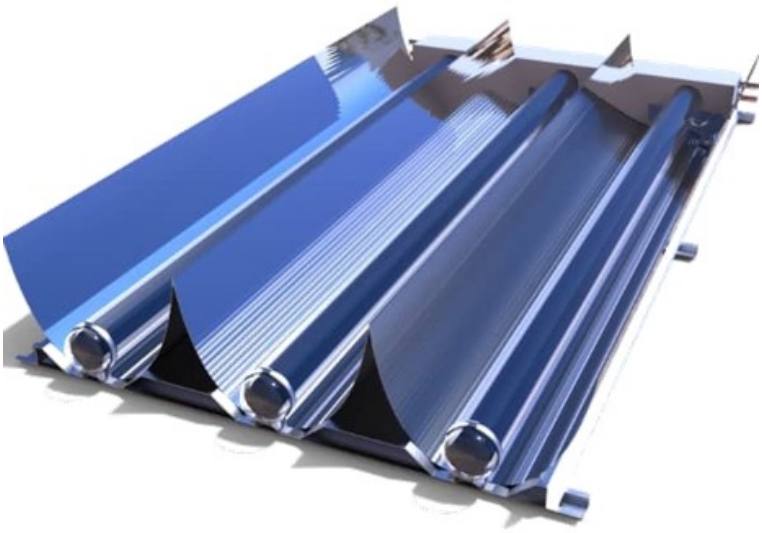

FIGURE 1.12: Commercial Segmented Solar Concentrator Produced by Artic Solar. Diagram from Artic Solar (http://www.articsolar.com/)

In order to test the theoretical efficiency of various segmented solar concentrator designs, a ray tracing model was implemented in Matlab. This ray tracing procedure is described in the next section.

Chapter 2

Computational Framework

The first chapter detailed the ideal design of ideal solar thermal concentrators. Some limitations to this design were mentions in section 1.2.7 and some current manufacturing solutions to these limitations was discussed in section 1.2.8, which included segmented solar concentrators. However, the theoretical efficiency of these concentrators has not been well studied. This chapter outlines a new computational approach and optimization to address design efficiency for various segmented solar concentrators setups under various constraints.

2.1 Shape Optimization Goals

Our main objective goals are to produce segmented solar thermal concentrators configurations that are:

- Easy to manufacture
- Adaptable to different design criteria
- Highly efficient, optimal, and practical
- Optimized by a computationally fast approach
- Robust to manufacturing errors

Although ideal 2D CEC designs exist, the performance of these designs quickly changes when the concentrator is approximated by segmented collocated linear segments. We aim to remove the limitations of continuously varying shapes and 2D designs by taking a computational approach.

This approach includes optimizing segmented solar concentrator efficiency for a given number of segments. The result is a design that is relatively easy to manufacture, while maximizing efficiency for the given design constraints.

Hence one of the primary goals is to achieve a concentrator design that can be manufactured cheaper while minimally sacrificing on concentrator efficiency. We call such concentrators to be optimal. They are no longer ideal in terms of collecting every ray that enters

the aperture, but they give the highest optical concentration ratio efficiency for the given design parameters.

2.1.1 Easy to Manufacture

The primary advantage of linear segmented collocated concentrators is that they are easy to manufacture. There are many factors that may contribute to the overall manufacturing cost and ease. Some of these factors include:

- Linear segments instead of curved surfaces
- Low number of segments
- Symmetric
- Concentrator wing lengths
- Aperature size
- Absorber shape
- Concentrator interior angles

2.1.2 Adaptable to Various Design Criteria

In addition to being easy to manufacture, concentrator designs should be adaptable to various design parameters. Many of these parameters may be chosen with manufacturing ease in mind. Many parameters may have constraints which represent manufacturing limits or other design preferences such as to meet space constraints.

- Trough or basic concentrator shape configurations
- Fixed number of segments
- Fixed wing lengths
- Maximum or fixed Aperature size
- Maximum concentrator width and length

2.1.3 Highly efficient, Optimal, and Practical

Concentrator designs should also be highly efficient and practical. Some aspects of design which ensure that configurations are highly efficient within the specified parameter limits include:

- Optimized concentrator configuration under given constraints

- At least or more efficient than segmented linear collocated concentrators with vertices placed along the ideal
- Convex

2.1.4 Optimized by a computationally fast approach

The optimizer used to determine the optimal concentrator configuration should be fast while giving good results. A few things that we implimented to increase computational speed were:

- Vectorized ray tracer
- Single software for both ray tracer and optimizer to reduce communication lag between various softwares

2.1.5 Robust to manufacturing errors

Finally, robustness is a requirement since small manufacturing errors should not result in large efficiency losses.

- Limited efficiency losses with small design errors
- Inherent manufacturing errors do not compromise concentrator efficiency

2.2 Other Computational Optimization Work in Nonimaging Optics

There has been a lot of optimization work done on continuum descriptions, which are very different in nature physically. In contrast, there has not been much research on shape optimization with particles in open source literature. Most commercial ray tracing software is not designed for optimization and is designed only for point sources, instead of a continuous source. The particle ray tracing model described in this paper uses extended sources and integrates optimization into the same software as the ray tracing program. The combined particle ray tracing gradient-free optimization method described in this paper has not previously been employed to optimize nonimaging solar thermal concentrators.

We give an explicit method and optimization framework approach for nonimaging optic concentrator designs. We show that generalized pattern search is effective for optimizing nonimaging designs. We particularly show it's effectiveness for low degree of segmented reflectors. Then we use our method to draw conclusions on sensitivity analysis of various concentrator designs.

A few problems that naturally arise that are unique to this optimization problem are local minima and discretization. These are nontradiational optimization shape optimization problems in the fact that they are discretized, have a ray tracer, the objective functions are

locally flat and require derivative-free optimization methods. The ray tracer must also deal with extended sources. We can also deal with enforcing convexity of shape by using pattern search.

Some design work in the field of nonimaging optics has been done using the simultaneous multiple surfaces (SMS) optical design method (Gimenez-Benitez et al., 2004). The software implementing the SMS is proprietary of Light Prescriptions Innovators. The formalism for the SMS is given in several papers.

Another formalism called the "Iterative generalized functional method of nonimaging optical design" is described by Bortz and Shatz, 2007 and is implemented in a code called NICOS (Shatz et al., 2008). Other work has been done on free-form surfaces for nonimaging optics by Miñano et al., 2009.

The published work of the above mentioned groups describe formalisms that are amiable to design. However, explicit methods are not given since their methods for nonimaging optics designs has been implemented in proprietary softwares. We propose a method for optimization approach for nonimaging optics and provide a complete explanation of the method and implementation in this paper.

Marston, Daun, and Collins, 2010 present an optimization algorithm for designing and optimizing concentrating solar collectors. They provide open source code for their method, which includes stochastic ray tracing in Matlab and stochastic gradient-based optimization using the modified Kiefer–Wolfowitz algorithm.

However, the authors admit that trials often fail to reach an optimum using the quadratic line search. An insufficiently smooth objective function and regions far from optimal with near-zero gradient are two suspected reasons that result in non-convergence. Furthermore, their chosen segmented solar concentrator setup only reached efficiencies of about 30% (Marston, Daun, and Collins, 2010).

They presented an explicit optimization method for various classes of nonimaging solar concentrators, but the unsuitable choice of gradient-based optimization sometimes produced impractical low performing designs. The other concentrating designs that were tested were smooth curves that varied parameters of a family of functions. Such designs do not have any apparent advantage over ideal concentrators in terms of efficiency nor reductions in manufacturing costs.

Other groups explicitly propose designs aimed at reducing manufacturing costs through the concatenation of a limited number of truncated cones (Jafrancesco et al., 2012). They demonstrate that a truncated cone approximations with joints along the ideal concentrator do not result in severe efficiency losses. However, they never optimize the cone joint locations and the focus of their application is for use with heliostat fields.

2.3 Concentrator Configuration

We considered several different configurations of nonimaging concentrators. We will first discuss what we will call the basic concentrator setup shown in Figure 2.1, which shares

many things in common with the other designs.

2.3.1 Basic Concentrator Setup

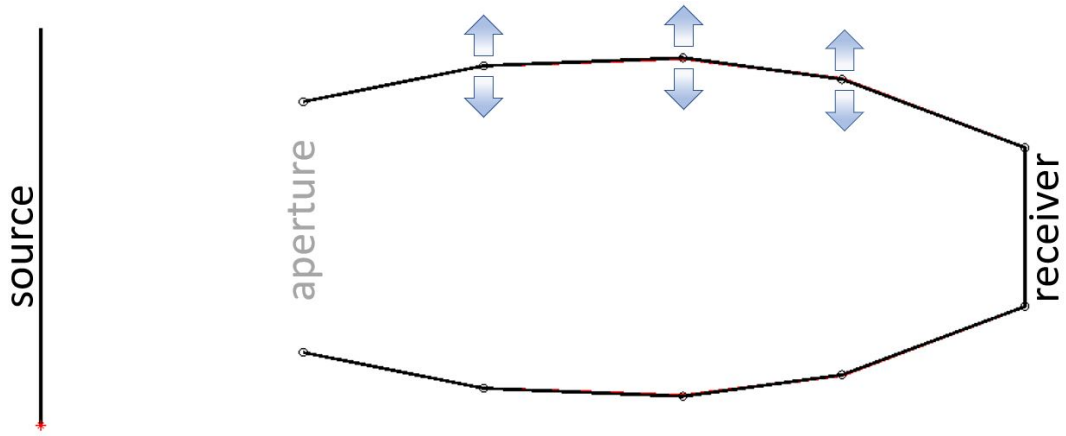

FIGURE 2.1: Basic concentrator setup with linear source on left and linear collocated concentrator segments on the right. The linear receiver, aperture, and source are all considered to be fixed. The interior vertices are allowed to move vertically up and down until an optimal concentrator configuration is found.

A source on the left sends rays into the aperture, or opening of the concentrator. The rays then reflect off of the linear collocated concentrator segments until they are either rejected back out through the aperture or reach the receiver. The source, aperture, and receiver are all considered fixed. Hence the vertices on each size of the aperture and the receiver are considered fixed as well.

The other interior vertices are free to move into a configuration that maximizes the percent of rays reaching the receiver from the source. The vertices may move only vertically, as shown by the arrows in the basic concentrator setup of Figure 2.1, or vertex location may be allowed to move both vertically and horizontally, depending on user preference. Vertically and horizontally moving vertices is one configuration variation of the basic concentrator setup, which only permits vertical variation.

Allowing more flexibility of vertex movements increases the number of degrees of freedom in the optimizer and hence increases optimization difficulty. The process of optimizing the location of these vertices will be discussed in the next chapter.

2.3.2 Increasing Vertices

With the basic concentrator setup selected, the number of concentrator vertices can be gradually increased incrementally. When a large number of vertices is given to the optimizer,

the initial placement of the vertices heavily influences the final optimal configuration found. The heavy influence of the prior placement of the vertices to the final optimal location found means that the initial vertex placement fed into the optimizer should not be arbitrary, but should be rather good, although not optimal.

One way to ensure that the initial placement of vertices fed into the optimizer is not vastly far away from concentrator configurations of high efficiency is to start with a low number of vertices which can be more easily optimized with less influence of the prior and incrementally increase the number of vertices after an optimal configuration is found at each stage. We will describe the process starting with three vertices, or meaning just one interior vertex to be optimized.

The y coordinate placement of the single interior vertex is initially optimized. The x coordinate is placed equidistant between the x coordinate of that of the aperture and receiver vertices. The number of interior vertices is then increased by creating a Piecewise Cubic Hermite Interpolating Polynomial, defined as pchip in Matlab, through the initial three vertices and placing two interior vertices whose x coordinates are equally spaced between the x coordinates of the aperture and receiver vertices. Therefore the total number of vertices on each concentrator wing is increased to four with one on the aperture, two interior vertices, and one on the receiver.

The concentrator with initial two interior y vertex placement located along the interpolated Piecewise Cubic Hermite Interpolating Polynomial is then optimized. Again, the Piecewise Cubic Hermite Interpolating Polynomial can be used to find the location of three interior y vertex placement locations with x coordinate placement equally spaced between the aperture and receiver x coordinate vertex locations. These interpolant vertex locations may be used as the initial vertex placement for the next optimization iteration. This process continues until the desired number of vertices is reached and ensures that initial vertex configurations are not vastly far away from efficient configurations.

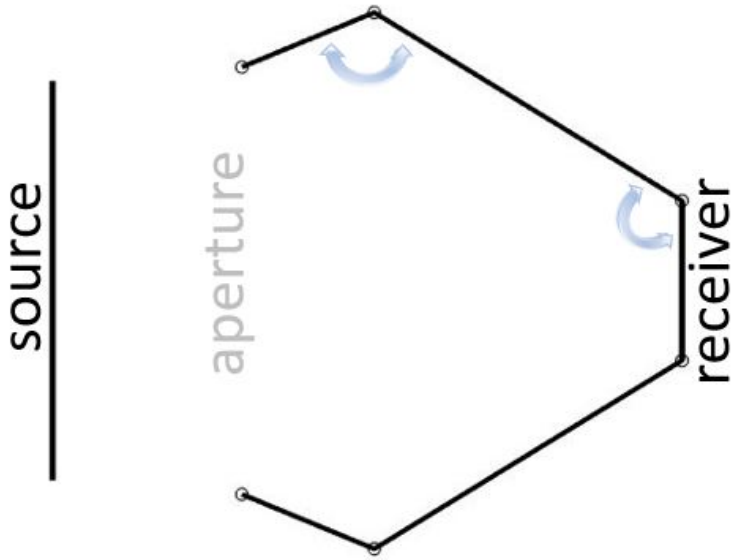

FIGURE 2.2: Basic concentrator variation with linear source on left and linear collocated concentrator segments on the right. The linear receiver and source are considered to be fixed. The interior angles are allowed to move until an optimal concentrator configuration is found.

2.3.3 Interior Angle Optimization

Instead of optimizing vertex locations and allowing concentrator segment lengths to vary, such as in the basic concentrator design given in Figure 2.1, an alternative concentrator configuration is to fix individual concentrator segment lengths and optimize the interior angle between adjacent segments, such as is shown in Figure 2.2. In this configuration the aperture is not considered fixed and becomes wider or narrower depending on the optimized interior angles.

2.3.4 Trough Concentrator Configuration

The interior angle optimization can be combined with either a flat absorber, as is shown in Figure 2.2, or a circular absorber, such as is shown in Figure 2.3. The linear absorber is conformed into a circular segmented absorber along with several concentrator segments along an approximate involute.

This configuration is particularly useful for trough concentrator designs whose absorber has a flowing material, such as oil or sand, encompassed within a vacuum tube. Tubular absorbers are the most commonly deployed design in practice.

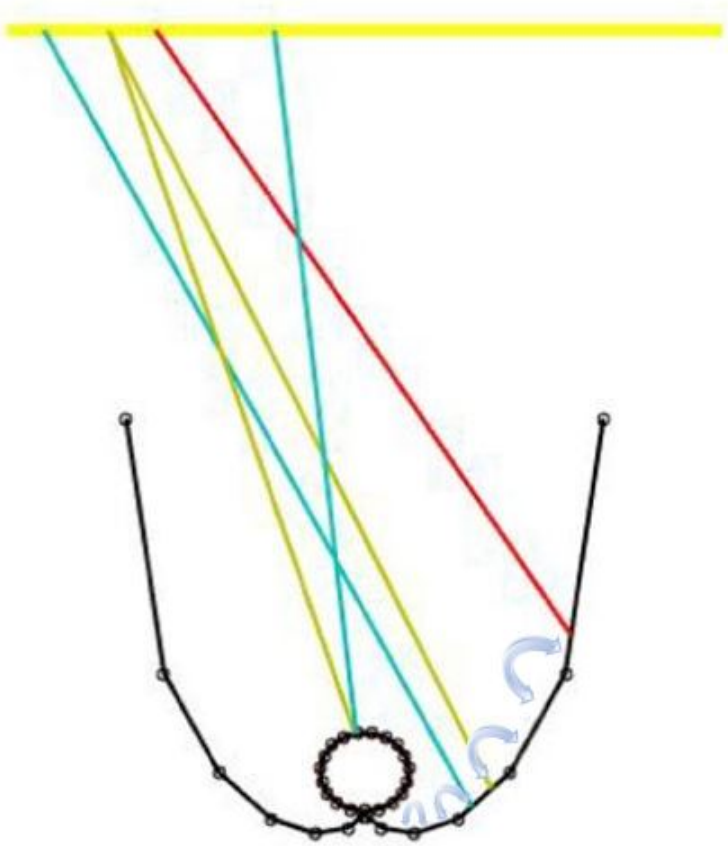

FIGURE 2.3: Basic concentrator variation with linear source above and trough collocated concentrator below with circular receiver. The circular receiver and linear source are considered to be fixed. The interior angles are allowed to move until an optimal concentrator configuration is found.

2.4 Objective Function and Constraints

As shown in Figure 2.1 for the basic concentrator setup, the vertices on each size of the aperture and the receiver are considered fixed. The other vertices are free to move to a configuration that maximizes the percent of rays reaching the receiver. The position of the interior vertices is denoted by, $\tilde{\mathbf{x}}$, which may include only the y-coordinate values if the x-coordinate values are to remain fixed or $\tilde{\mathbf{x}}$ may concatenate x- and y-coordinate values so the placement of both are optimized.

If the placement of the x-coordinate values are also to be optimized, some constraints on the possible location of the x-coordinates is placed to prevent consecutive points from crossing one another. For example, we initially placed the x-coordinate values at evenly

spaced points between the aperture and receiver. One such constraint that we implemented was to prevent points from crossing one another was to put a lower bound and upper bound on the optimized x-coordinate location. The lower bounds were set as the midpoint between the current x-value vertex coordinate and the x-coordinate of the previous vertex. Similarly, the upper bounds were set as the midpoint between the current x-value vertex coordinate and the x-coordinate of the next vertex.

2.4.1 Defining the Objective Function

The objective is to place the movable vertices in positions that maximize the number of rays hitting the receiver that enter the aperture, which is similar to maximizing the optical efficiency as defined in equation (1.9). However, most optimization methods seek to minimize, not maximize, the objective function. Hence we turn this maximization problem into a minimization problem by minimizing the additive inverse of the optical concentration ratio, meaning our objective function to minimize becomes,

$$F(\mathbf{x}) = -\frac{(\text{number of rays collected on the receiver})}{(\text{total number of rays entering concentrator})} \tag{2.1}$$

where the vector $\mathbf{x} = (\mathbf{x_1}, \mathbf{x_2}, \mathbf{x_3}, ..., \mathbf{x_m})$ contains the coordinate points of the vertices of the top polygonal reflector. We enforce symmetry, meaning that the points of the vertices on the lower polygonal reflector are given by $\mathbf{x} = (-\mathbf{x_1}, -\mathbf{x_2}, -\mathbf{x_3}, ..., -\mathbf{x_m})$.

The total number of rays entering the concentrator is proportional to the incoming radiation flux. The proportional flux is what is measured on the absorber. The numerator of equation 2.1 is the flux of radiation entering the aperture and the denominator is the flux of radiation incident on the absorber. Hence the ratio of the collected flux on the absorber over the total flux entering the concentrator is maximized.

For an ideal concentrator, $F(\mathbf{x}) = -\mathbf{1}$, meaning that all of the rays entering the solar thermal concentrator are collected at the receiver. Since the ideal concentrator is a smooth continuous curve, the discretized linear segmented solar thermal concentrator objective function $F(\mathbf{x})$ will only approach -1 as the number of polygonal reflector vertices (i.e. length of $\mathbf{x}$) tends to infinity.

We are primarily interested in segmented solar thermal concentrators with low numbers of segments on each wing. In this case we are far from configurations that closely represent the ideal concentrator. Hence the ideal configuration may not be vertices placed exactly along the ideal concentrator.

In optimizing the location of concentrator vertices, we will discuss the advantages and pitfalls of various optimization techniques and why pattern search was ultimately found to best deal with segmented solar concentrator optimization difficulties.

2.4.2 Constraints

We implement constraints which enforce convexity. Without such constraints, we found that the optimizer sometimes becomes stuck in non-convex designs. We only consider convex designs to be practical and therefore implement a convexity constraint.

We have nonlinear constraints to enforce convexity implemented as,

$$c = \frac{1}{2} - \text{all}(d_i < 0) \tag{2.2}$$

where d_i are determinants of consecutive concentrator segment vectors. Consecutive concentrator segment vectors are referred to as the vectors formed between consecutive vertices, such as $\vec{v_1} = \begin{bmatrix}(x_2 - x_1)\\(y_2 - y_1)\end{bmatrix}$ and $\vec{v_2} = \begin{bmatrix}(x_3 - x_2)\\(y_3 - y_2)\end{bmatrix}$ where (x_1, y_1), (x_2, y_2), and (x_3, y_3) are consecutive concentrator vertices as shown in Figure 2.4. When the concentrator is convex, the sign of the determinant will be negative since $\sin\theta < 0$ where θ is the angle between $\vec{v_1}$ and $\vec{v_2}$.

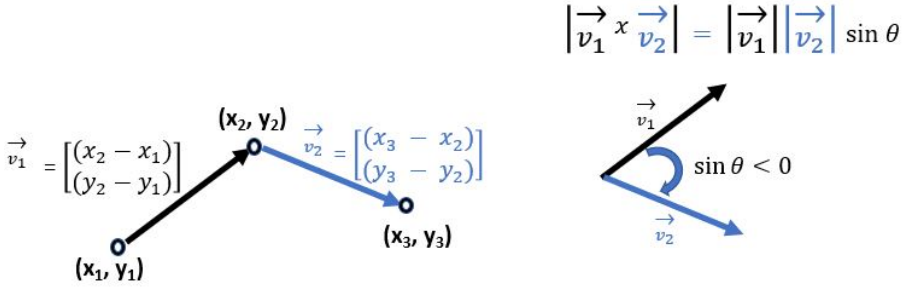

FIGURE 2.4: This figure shows how the signed angle between consecutive concentrator segment vectors is negative when that portion of the concentrator is convex.

By a similar argument, if a portion of the concentrator is concave, such as that shown in Figure 2.5, then the sign of the determinant will be negative since $\sin\theta > 0$ where θ is the angle between $\vec{v_1}$ and $\vec{v_2}$.

Another way to write the determinants of consecutive concentrator segment vectors is,

$$d_i = \Delta x_{i-1}\Delta y_i - \Delta x_i \Delta y_{i-1} \tag{2.3}$$

where

$$(\Delta x_j, \Delta y_j) = (x_j, y_j) - (x_{j-1}, y_{j-1}) \tag{2.4}$$

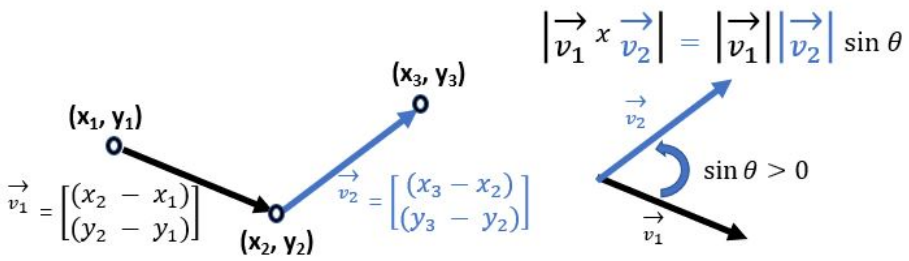

FIGURE 2.5: This figure shows how the signed angle between consecutive concentrator segment vectors is positive when that portion of the concentrator is concave.

The convexity constraint may also be written mathematically as,

$$c = \frac{1}{2} - \Pi_{i=1}^{n}(1 - H(d_i)) \tag{2.5}$$

where H is the heavyside function that is one if d_i is less than zero and and zero if d_i is greater than zero. Hence equation (2.5) is $\frac{1}{2}$ when all concentrator segments are aligned in a convex arrangement and $-\frac{1}{2}$ when any two consecutive segment arrangement is concave.

Upper bound constraints can also be placed on the y coordinate values to prevent vertices on the concentrator wings from being too far away from the center axis. Such constrainst can also prevent interior angle optimized concentrators from opening too wide or becoming too flat.

2.5 Source Ray Distribution and Number of Rays

Rays originate from all points along the linear source. However, coding requires discretization, meaning rays originate from several fixed points along the linear source. The various options for discretized light generation are described below.

2.5.1 Adaptive Source

The optimizer performs the best when starting with a limited number of degrees of freedom and gradually incrementing the degrees of freedom following each consecutive optimization. However, since additional degrees of freedom will be added, it is not always necessary to find the most optimal configuration for lower degrees of freedom. Using fewer rays may be adequate to achieve a sufficiently efficient design, even if it is not the most optimal for that many vertices. Additional vertices may then be added using this sufficiently optimal design. As the number of degrees of freedom, and hence the computational complexity, increases, the number of rays also increases for increased precision.

Hence it may be desired to progress through the concentrator configurations of lower degrees of freedom more quickly so that the majority of computational time can be spent optimizing higher degree concentrator configurations. In order to find a sufficiently optimal design with fewer computing resources, the number of rays sent through low degree concentrators can be reduced.

When the number of rays sent through the concentrator depends on the number of degrees of freedom to be optimized, we call the source adaptive. An adaptive source changes based on the degrees of freedom and sends more rays through the concentrator for harder to optimize, higher degree concentrator configurations.

Let N_{joints} be the number of vertices, or joints, along the top portion of the concentrator. For an adaptive source, the number of sources, $N_{sources}$, along the linear source is given by,

$$N_{sources} = N_{joints} \times SPJ \tag{2.6}$$

Where SPJ, the number of sources per joint is defined by the user. SPJ is typically small, such as 2, to increase speed. The number of sources is defined as the number of discrete source points along half of the linear source. The number of sources are evenly distributed along the bottom half of the linear source from the lowest endpoint of the source to the center.

Since symmetry is enforced, the upper and lower portions of the concentrator are reflectionally symmetric around the central axis of the concentrator. Hence rays sent from the top half of the source and the bottom half of the source will trace out reflectionally symmetric paths. Since the ultimate destination of reflectionally symmetric rays is the same, meaning either both reach the receiver or both are rejected and escape back through the aperture, the destination of only one of the rays needs to be calculated by the ray tracer.

2.5.2 Fixed Source

An alternative way to define the number and position of rays generated from the linear source is to use what we call a fixed source. A fixed source gets its name from the fact that the number of rays sent through the concentrator for an optimization is fixed and does not depend on the optimizer number of degrees of freedom. Hence, the number of sources is given by,

$$N_{sources} = K_{fixed} \times SPJ \tag{2.7}$$

where K_{fixed} is a fixed constant, which we often choose to be 100.

For both the fixed and adaptive sources, the number of rays emanating from each source is given by $N_{angles} = N_{sources}$. The angles are evenly distributed between the minimum and maximum angle values of rays that may enter the concentrator. Hence the total number of rays that are traced through the concentrator is given by,

$$N_{rays} = N_{sources} \times N_{angles} \tag{2.8}$$

2.5.3 Lambertian Source

The radiance from the sun is approximately a Lambertian emitter. A Lambertian emitter has the property that it's luminance is isotropic, meaning there is equal irradiance from any angle when viewed at an equal distance from the source.

However, the intensity is proportional to the cosine of the angle with respect to the central concentrator axis. Hence rays hitting the absorber are weighted with respect to the cosine of their original theta values to imitate a Lambertian source in the following way,

$$F(\mathbf{x}) = \frac{(\text{number of rays collected on the receiver})}{(\text{total number of rays entering concentrator})} \frac{\cos\left(\theta_{\mathbf{initial}}\right)}{\sum \cos\left(\theta_{\mathbf{initial}}\right)} \tag{2.9}$$

Hence the rays incident on the absorber are weighted according to the cosine of their origination angle from the source with respect to the concentrator. Equation 2.9 is essentially a rescaled version of the objective function defined in equation 2.1.

The concentrator mirrors are assumed to be specular, not Lambertian, reflectors. Therefore all mirror reflections are calculated using Snell's Law.

2.6 Ray Tracing Basic Setup

Following standard ray tracing algorithms, rays originate at a source, such as the sun, and are traced through the concentrator until the rays are either absorbed by the receiver or escape back through the aperture. Since the distance from the sun to the concentrator is unproportionally large compared to the magnitude of the dimensions of the concentrator, the rays of the sun are instead modeled to be coming from a linear segment positioned close enough to the concentrator that both can be fully viewed with a reasonably sized viewing window.

The ray tracer is vectorized in Matlab and is highly efficient. The ray tracer communicates directly with the built-in Matlab optimizers, decreasing communication lag between platforms.

2.6.1 Ray Origination

Ray originate from N distinct points on the linear source segment, each point emitting rays at N distinct angles θ. These angles are distributed according to a Lambertian source, meaning that in general the rays are forward-peaked. For example, a ray originating from a point $\begin{bmatrix} x_0 \\ y_0 \end{bmatrix}$ on the source travels in an initial direction θ_i.

2.6.2 Ray Intersection with Concentrator

The ray then travels some distance t before intersecting with segment on the segmented solar thermal concentrator, meaning the new ray location is at $\begin{bmatrix} x_0 + t\cos(\theta_i) \\ y_0 + t\sin(\theta_i) \end{bmatrix}$. The ray

passes through the aperture and continues until it strikes either the absorber or one of the flat reflective segments of the concentrator. Since the ray is only permitted to propagate forwards, $t > 0$.

The initial concentrator configuration is determined by the coordinates of a specified number of joints that will connect consecutive flat reflective segments. The x-values of these points is determined by taking a vector of equally spaced points between the x-values of the aperture and absorber. The y-values are initially determined by those on a straight line connecting the top aperture point and the top most point on the absorber.

Since the concentrator is made out of linear line segments, the segments of the concentrator are described by $\begin{bmatrix} x_A(1-s) + x_B s \\ y_A(1-s) + y_B s \end{bmatrix}$ where $0 \leq s \leq 1$. Hence (x_A, y_A) is one segment endpoint and (x_B, y_B) is the other. The intersection of the ray with a segment of the concentrator is be described by,

$$x_0 + t\cos(\theta_i) = x_A(1-s) + x_B s \tag{2.10}$$

$$y_0 + t\sin(\theta_i) = y_A(1-s) + y_B s \tag{2.11}$$

Rearranging, we achieve,

$$\begin{bmatrix} x_0 - x_A \\ y_0 - y_A \end{bmatrix} = s \begin{bmatrix} x_B - x_A \\ y_B - y_A \end{bmatrix} - t \begin{bmatrix} \cos(\theta_i) \\ \sin(\theta_i) \end{bmatrix} \tag{2.12}$$

This can be written in the matrix form,

$$\begin{bmatrix} x_0 - x_A \\ y_0 - y_A \end{bmatrix} = \begin{bmatrix} -\cos(\theta_i) & (x_B - x_A) \\ -\sin(\theta_i) & (y_B - y_A) \end{bmatrix} \begin{bmatrix} t \\ s \end{bmatrix} \tag{2.13}$$

Since we are interested in the values of t and s to determine the distance the ray traveled before hitting a receiver segment and to also determine the location of intersection between the ray and the receiver, we invert the matrix in Equation 2.13 to yield,

$$\begin{bmatrix} t \\ s \end{bmatrix} = \frac{1}{\sin(\theta_i)(x_B - x_A) - \cos(\theta_i)(y_B - y_A)} \begin{bmatrix} (y_B - y_A) & -(x_B - x_A) \\ \sin(\theta_i) & -\cos(\theta_i) \end{bmatrix} \begin{bmatrix} x_0 - x_A \\ y_0 - y_A \end{bmatrix} \tag{2.14}$$

There will be one unique pair of t and s values satisfying the conditions $t > 0$ and $0 \leq s \leq 1$ corresponding to the unique segment of intersection of the ray and the receiver. Due to numerical precision issues, after the initial reflection with a segment on the receiver, this segment is excluded from the next ray-receiver intersection calculation. This means that a ray can not intersect with the same segment on the receiver twice consecutively.

2.6.3 Updating Ray Position and Propagation Angle

When a ray intersects with the receiver, it can either strike the concentrator on the top half portion while traveling from left to right, strike the bottom half of the concentrator while traveling from left to right, strike the top half of the concentrator while traveling from right to left, or strike the bottom half of the concentrator while traveling right to left. These four scenarios are described in the following sections.

Ray Strikes Concentrator Top Traveling Left to Right

Figure 2.6.3 describes a light ray, shown by a yellow dashed line, intersecting with a receiver segment, shown by a solid black line. The light dashed yellow ray shows the direction path of the ray, had it not intersected with the receiver and θ_i is the angular direction of the ray initially with respect to the horizontal.

Upon reflection with the receiver segment, θ_r describes the new angular direction of the ray. The inward pointing normalized vector normal to the receiver segment, $\overrightarrow{N}$, is denoted by a blue solid line. The red angle denoted by π is the angle of incidence. While the angle of incidence is equal to the angle of reflection, note that in our depiction, $\pi \neq \theta_r$ since here π is a relative angle of the incident ray with respect to the normal, whereas θ_r is an absolute angle with respect to the horizontal.

From Figure 2.6.3 we see that $\rho_i = \pi - \alpha_i$ and that $\cos(\alpha_i) = \overrightarrow{N} \cdot \begin{bmatrix} \cos(\theta) \\ \sin(\theta) \end{bmatrix}$ where $\overrightarrow{N}$ is the inward pointed normalized vector normal to the solid black concentrator segment. Hence,

$$\begin{aligned} \theta_r &= \theta_i + \pi + 2\rho_i && (2.15)\\ &= \theta_i + \pi + 2\pi - 2\alpha_i && (2.16)\\ &= \theta_i + \pi - 2\alpha_i && (2.17)\\ &= \theta_i + \left(\pi - 2\arccos\left(\overrightarrow{N} \cdot \begin{bmatrix} \cos(\theta) \\ \sin(\theta) \end{bmatrix}\right)\right) && (2.18)\\ & && (2.19) \end{aligned}$$

Ray Strikes Concentrator Bottom Traveling Left to Right

From Figure 2.6.3 we see that again $\rho_i = \pi - \alpha_i$ and that $\cos(\alpha_i) = \overrightarrow{N} \cdot \begin{bmatrix} \cos(\theta) \\ \sin(\theta) \end{bmatrix}$ where $\overrightarrow{N}$ is the inward pointed normalized vector normal to the solid black concentrator segment. Hence,

$$\theta_r = \alpha - (2\pi - \theta_i) - \rho_i \tag{2.20}$$
$$= \theta_i - \pi + 2\alpha_i \tag{2.21}$$
$$= \theta_i - \left(\pi - 2\arccos\left(\overrightarrow{N} \cdot \begin{bmatrix}\cos(\theta)\\ \sin(\theta)\end{bmatrix}\right)\right) \tag{2.22}$$
$$\tag{2.23}$$

Ray Strikes Concentrator Top Traveling Right to Left

From Figure 2.6.3 we see that again $\rho_i = \pi - \alpha_i$ and that $\cos(\alpha_i) = \overrightarrow{N} \cdot \begin{bmatrix}\cos(\theta)\\ \sin(\theta)\end{bmatrix}$ where $\overrightarrow{N}$ is the inward pointed normalized vector normal to the solid black concentrator segment. Hence,

$$\theta_r = \theta_i + \alpha - \rho_i \tag{2.24}$$
$$= \theta_i - \pi + 2\alpha \tag{2.25}$$
$$= \theta_i - \left(\pi - 2\arccos\left(\overrightarrow{N} \cdot \begin{bmatrix}\cos(\theta)\\ \sin(\theta)\end{bmatrix}\right)\right) \tag{2.26}$$
$$\tag{2.27}$$

Ray Strikes Concentrator Bottom Traveling Right to Left

From Figure 2.6.3 we see that again $\rho_i = \pi - \alpha_i$ and that $\cos(\alpha_i) = \overrightarrow{N} \cdot \begin{bmatrix}\cos(\theta)\\ \sin(\theta)\end{bmatrix}$ where $\overrightarrow{N}$ is the inward pointed normalized vector normal to the solid black concentrator segment. Hence,

$$\theta_r = \theta_i - \alpha + \rho_i$$
$$= \theta_i + \pi - 2\alpha$$
$$= \theta_i + \left(\pi - 2\arccos\left(\overrightarrow{N} \cdot \begin{bmatrix}\cos(\theta)\\ \sin(\theta)\end{bmatrix}\right)\right)$$

In summary, the cases can be divided into the following two groups:

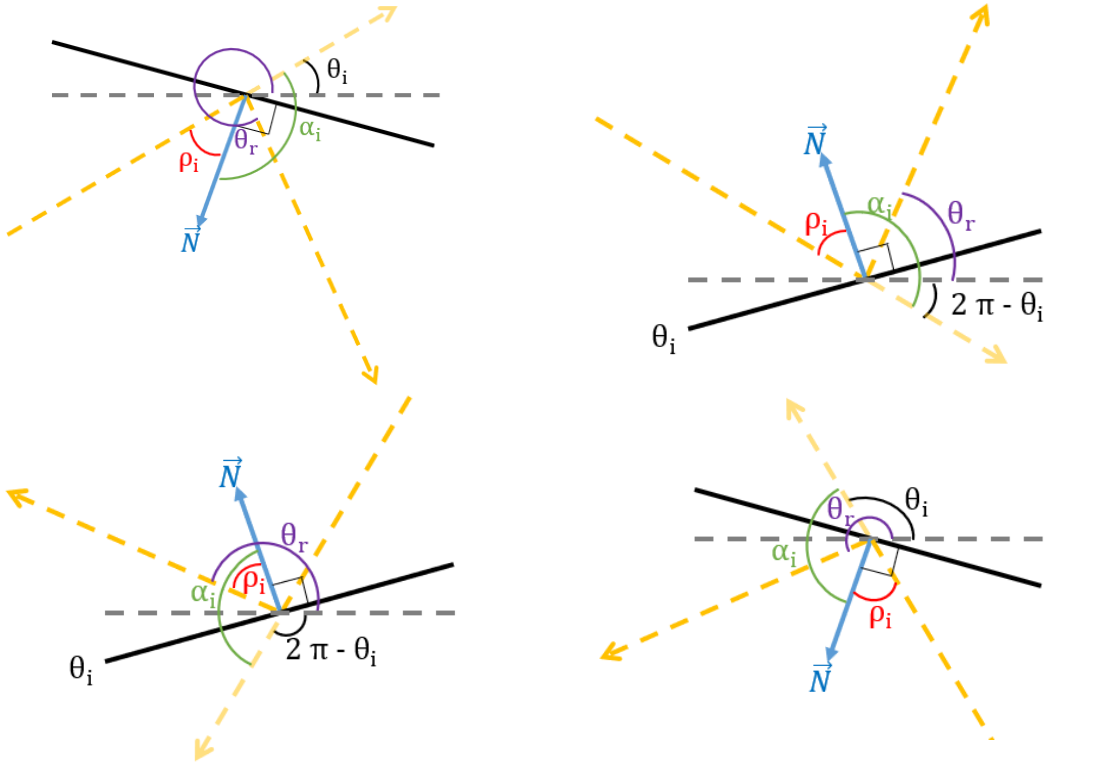

$$\theta_r = \theta_i + \left(\pi - 2\arccos\left(\vec{N}\cdot\begin{bmatrix}\cos(\theta)\\ \sin(\theta)\end{bmatrix}\right)\right)$$

$$\theta_r = \theta_i - \left(\pi - 2\arccos\left(\vec{N}\cdot\begin{bmatrix}\cos(\theta)\\ \sin(\theta)\end{bmatrix}\right)\right)$$

Overall the formula for the angle of reflection of any ray with concentrator can be defined as,

$$\theta_r = \theta_i - \text{sign}\left(\vec{N}x\begin{bmatrix}\cos(\theta)\\ \sin(\theta)\end{bmatrix}\right)\left(\pi - 2\arccos\left(\vec{N}\cdot\begin{bmatrix}\cos(\theta)\\ \sin(\theta)\end{bmatrix}\right)\right)$$

The reflection angle defines the current propagation angle. The location of the rays are then updated to the location of the intersection of each ray with the receiver. The updated location, (x, y), serves as a starting point of the ray in the current propagation direction, θ, which is defined by the reflection angle.

Each ray then again propagates a distance, t, before again intersecting with a segment on the segmented solar thermal concentrator, the receiver, or passing back through the aperture. Due to round-off errors, it is possible to get propagation distance around $t = 10^{-16}$ in which a ray intersects with the same segment twice. Since such a scenario is not physically possible or desired, a ray is restricted from intersecting the same segment twice consecutively.

Once a ray intersects either the receiver or the aperture, this final destination is recorded

and that particular ray is then removed from ray tracing algorithm. The ray tracing algorithm continues until all rays have either been collected at the receiver or escaped back through the aperture.

After the fate of all rays entering the concentrator has been determined, the objective function is calculated based on the total number of rays collected on the receiver versus the total number of rays that entered the concentrator aperture. The objective function value for the given concentrator configuration input is then communicated to the optimizer to assign an efficiency value for the given design.

Chapter 3

Concentrator Optimization Methods

In this section we will begin by discussing gradient based optimization and why gradient based methods fail in our particular case given the objective function behavior. Then we will discuss a derivative-free optimization approaches to optimizing such problems. We will primarily focus on the derivative free optimization approach called pattern search and the derivative free prequels leading up to the development of the pattern search optimization program.

3.1 Gradient Based Optimization and Its Failure

Standard techniques for optimization are gradient based. Some gradient based techniques include line search, trust region methods, conjugate gradient, and Quasi-Newton. These methods either directly compute or estimate the gradient (Nocedal and Wright, 2006).

Initially, a gradient based solver in Matlab, fmincon, which is a nonlinear programming solver was implimented. However, this algorithm was ineffective at finding a minima. For any vector input, $\mathbf{x}$, of initial concentrator vertices, fmincon would immediately terminate, stating that the gradient was already smaller than tolerance. This suggests that $F(\mathbf{x})$ is "flat" with respect to small variation in $\mathbf{x}$, meaning fmincon is content with any initial shape.

Furthermore, our objective function is not differentiable and changes in any vertex may completely change which rays reach the receiver and which ones do not. Since each vertex controls the location and orientation of the adjacent flat reflector segments, changing one vertex changes the direction in which rays reflect off these two reflector surfaces, which in turn changes their total paths thereafter. Rays that had previously been collected by the receiver may now be rejected, and conversely some rays that had previously been rejected may now be collected.

Since such a large number of ray paths are altered drastically by a change in location of any vertex, we can not effectively compute a gradient. Hence, all gradient based methods are likely to fail. The fmincon interior point function uses the Rosebrock function as a performance test. This gradient was sufficiently close to zero, thus halting any improvements from being made from the initial configuration.

3.1.1 Nondifferentiability of Objective Function

As is discussed in the results section of the next chapter and shown in Figure 4.4, the simulated objective function is locally flat everywhere with abrupt jumps or discontinuities, meaning that the objected function is not differentiable. The scale on which these discontinuities occurs depends on the discrete number of rays originating from the source and the mesh scale at which we incrementally increase the y-coordinate values.

However, assuming an infinite number of rays are generated from the source and that the y-coordinates may be infinitesimally adjusted, the objective function may be continuous or must at least a piece-wise smooth, as shown previously. Each of the concentrator segments is piecewise smooth and we would expect the incoming flux of radiation from the source onto the receiver to change in a smooth manner. We expect that the flux, F, is a function of the shape, S, denoted by $F(S)$. We would also expect that a small perturbation in the shape would result in an equally small perturbation in flux on the receiver,

$$F(S_0 + \epsilon_{S_1}) \approx F(S_0) + \epsilon_{S_1} F'(S_0) \tag{3.1}$$

Where ϵ_{S_1} = perturbation to the shape S_0.

However, since we are not able to simulate an infinite number of rays originating from our source, nor are we able to infinitesimally increment our concentrator vertices, derivative-based methods will fail. Hence, we must turn to derivative-free alternatives.

3.2 Derivative-Free Optimization for Continuous Problems

Since gradient based methods were shown to be unsuccessful optimizing concentrator vertices, we turned to derivative-free optimization methods. Since our problem has a plethora of local minima, a derivative-free method would need to be effective in evading local minima traps. Furthermore, our objective function has several discontinuities, which often makes derivative-based methods unsuitable (Koziel and Yang, 2011).

In general derivative free methods are effective in avoiding local minima, able to obtain global minima, fast, and relatively easy to program. However, many derivative free methods are only effective for relatively low degrees of freedom.

Some derivative free models seek to minimize the objective function within a defined trust region. Others include simulated annealing, conjugate-direction methods, pattern search methods, and the simplex-reflection method of Nelder and Mead (Nocedal and Wright, 2006). Nelder Mead has a region whose average is minimized. However, it was later shown that Nelder Mead could fail to converge to a local solution even on a convex two-dimensional unconstrained minimization problem (Audet, 2014). The reason Nelder Mead may fail to converge to a minimum of the objective function is due to the the fact that the uniform linear independence property is not guaranteed to hold (Torczon, 1997).

3.2.1 Coordinate Search: The Prequel of Pattern Search

Another early type of derivative free optimization was coordinate search, which polled $2n$ trial points around the current iteration looking for improvement, or a point whose value was smaller that that of the current value. An advantage of such a method is that it did not require any kind of smoothness in the objective function, only that the objective function was defined at each of the polling locations. The polling locations were defined in the directions of the ith coordinate vector in $\mathbb{R}^n$ (Audet, 2014). The polling locations were located around the current iteration, x_k in the following manner:

$$P_k = x_k \pm \delta_k e_i : i = 1, 2, ..., n$$

Polling was considered successful if one of the polling points P_k was smaller than the current iterate x_k. After a successful poll, the current iterate then moves to the new smaller iterate P_k and $\delta_k > 0$ remains either unchanged during the next poll, or it increases by some expansion factor, such as a factor of 2. In an unsuccessful poll in which none of the polling points P_k is smaller than the current iterate x_k, then δ_k is decreased by some factor, such as decreased by a factor of $1/2$ (Conn, Scheinberg, and Vicente, 2009). The polling continues until δ_k is smaller than some specified tolerance.

3.3 Pattern Search

Coordinate search lead to the development of the class of pattern search algorithms. Pattern Search is also called Direct Search, terms first used by Hooke and Jeeves, 1961. Other names include Derivative-Free Search, or Black-Box Search and such techniques are primarily used on discontinuous or not differentiable objective functions. Pattern search algorithms expands the use and flexibility of coordinate search by removing the requirement that polling points exclusively be searched for strictly along coordinate bases.

Instead of coordinate bases in coordinate search, positive bases are used in pattern search, which are minimal sets of directions whose nonnegative linear combinations span $\mathbb{R}^n$ (Audet, 2014). Positive bases were first introduced into pattern search by Lewis, 1996. Positive basis are not basis since they likely over span $\mathbb{R}^n$. However, in this way only positive linear combinations need be considered. Another advantage of utilizing positive bases is that the algorithm may progress in the direction of steepest decent faster. The speed increase in computation time when moving more accurately along a direction of steepest decent generally outweighs the added computation at each step.

Another advantage of pattern search is its ability to adapt to landscape individual optimization problems. Different optimization problems will have different numbers of local minima with varying distances between these local minima. Ideally optimizers must resist setting in local minima so that the global minima may be obtained.

Another key difference between coordinate search and pattern search is that pattern search allows for the general coarsening or refining of the mesh through the introduction of

a mesh size adjustment parameter τ, such that

$$\delta_{k+1} = \tau^{r^k} \delta_0 \tag{3.2}$$

where r^k is some positive or negative integer that depends on the iteration number k. In order to converge, the sequence of mesh size parameters must satisfy the Mesh Gets Infinite Fine Theorem, (Audet and Hare, 2017), namely,

$$\lim_{k \to +\infty} \inf \delta_k = 0 \tag{3.3}$$

While Conn, Scheinberg, and Vicente, 2009 state that δ_k may increase after a successful poll, Audet, 2014 asserts that a defining difference between coordinate search and pattern search is the ability of δ_k to increase in pattern search after a successful poll. Increasing the mesh size parameter δ_k allows the algorithm to recover from a bad initial choice of the parameter δ_0 and avoid local minima.

Furthermore, pattern search is proven to have global convergence without the need of enforcing sufficient decrease in interates, such as fraction of Cauchy decrease, fraction of optimal decrease, or the Armijo-Goldstein-Wolf conditions (Torczon, 1997).

Although we do not utilize this method, there is an extension of the pattern search method which adds additional trial points on a mesh in a region $||x - x_k|| \leq C\Delta_k$, where x is from the mesh area, Δ_k is the frame size parameter, and C is defined in the directions of the positive basis spanning set. This method is called Mesh Adaptive Direct Search (MADS) and also includes implementation of stochasticity into the courseness of the polling search.

The key difference in MADS is that a new parameter called the frame size parameter, Δ_k is introduced. Instead of polling points only at mesh parameter distances δ_k along the positive bases, now a points along the positive bases within the frame size parameter $0 < \delta_k < \Delta_k$. A similar convergence requirement is that the frame size parameter sequence satisfies $\lim_{k \to +\infty} \inf \Delta_k = \lim_{k \to +\infty} \inf \delta_k = 0$ (Audet and Hare, 2017).

3.3.1 Polling Method

Pattern search polls the objective function, $F(\mathbf{x})$ on mesh points surrounding the current vertex value. For example, assume the vertex is initially placed at x_0 and polling takes place along coordinate bases for simplicity.

During the first iteration, the objective function, $F(\mathbf{x})$, is polled on the mesh points surrounding x_0 in the following manner,

$$\begin{aligned} &F(\mathbf{x_0} + \begin{bmatrix} 1 & 0 \end{bmatrix}) \\ &F(\mathbf{x_0} + \begin{bmatrix} 0 & 1 \end{bmatrix}) \\ &F(\mathbf{x_0} + \begin{bmatrix} -1 & 0 \end{bmatrix}) \\ &F(\mathbf{x_0} + \begin{bmatrix} 0 & -1 \end{bmatrix}) \end{aligned}$$

If $F(\mathbf{x_i}) < \mathbf{F}(\mathbf{x_0})$, the poll is considered successful.

After a successful poll, the point $\mathbf{x_0}$ is updated to the new point $\mathbf{x_1}$. The mesh in the next iteration is multiplied by an *Expansion Factor*. The default value is 2.

During the second iteration, the objective function is polled on the following mesh points surrounding x_1

$$F(\mathbf{x_1} + \mathbf{2} * \begin{bmatrix} 1 & 0 \end{bmatrix})$$
$$F(\mathbf{x_1} + \mathbf{2} * \begin{bmatrix} 0 & 1 \end{bmatrix})$$
$$F(\mathbf{x_1} + \mathbf{2} * \begin{bmatrix} -1 & 0 \end{bmatrix})$$
$$F(\mathbf{x_1} + \mathbf{2} * \begin{bmatrix} 0 & -1 \end{bmatrix})$$

If $F(\mathbf{x_i}) < \mathbf{F}(\mathbf{x_1})$, the search is successful. If $F(\mathbf{x_1}) < \mathbf{F}(\mathbf{x_i})$ for all $\mathbf{x_i}$ in the above four cases, the poll is considered unsuccessful.

After an unsuccessful poll, the current point remains the same, which in this case would mean $x_2 = x_1$. The mesh in the next iteration is then halved, or multiplied by an appropriate *Contraction Factor*.

In the third iteration, the objective function is polled on the mesh points surrounding x_2

$$F(x_2 + \frac{1}{2} * \begin{bmatrix} 1 & 0 \end{bmatrix})$$
$$F(x_2 + \frac{1}{2} * \begin{bmatrix} 0 & 1 \end{bmatrix})$$
$$F(x_2 + \frac{1}{2} * \begin{bmatrix} -1 & 0 \end{bmatrix})$$
$$F(x_2 + \frac{1}{2} * \begin{bmatrix} 0 & -1 \end{bmatrix})$$

The search continues until the difference between consecutive iteration points is smaller than tolerance value.

3.4 Stopping Criteria and Parameter Values

Pattern search terminates when one of the following scenarios occurs: the mesh size, step size or objective function value differences between consecutive points fall below defined parameter tolerance values, or if the maximum number of iterations, function evaluations or time limit have been exceeded (Works, 2020a).

Table 3.1 lists the default values of the pattern search algorithm parameters in Matlab that can be specified by the user.

Parameter	Default Value
AccelerateMesh:	0
ConstraintTolerance:	1.0000e-06
FunctionTolerance:	$1.0000e^{-06}$
InitialMeshSize:	1
MaxFunctionEvaluations:	'2000*numberOfVariables'
MaxIterations:	'100*numberOfVariables'
MaxTime:	∞
MeshContractionFactor:	0.5000
MeshExpansionFactor:	2
MeshTolerance:	$1.0000e^{-06}$
PollMethod:	'GPSPositiveBasis2N'
PollOrderAlgorithm:	'consecutive'
ScaleMesh:	1
StepTolerance:	$1.0000e^{-06}$
UseCompletePoll:	0
UseCompleteSearch:	0
UseParallel:	0
UseVectorized:	0

TABLE 3.1: The above table shows the Matlab pattern search parameters that can be changed by the user with the default values listed (Works, 2020b).

Pattern search is considered successful in finding an appropriately optimum value if the mesh size, step size or objective function value tolerances cause termination. On the other hand, pattern search may terminate but fail to find an appropriate optimum if the maximum number of iterations, function evaluations limit or time limit are exceeded. In these cases the result may not be sufficiently optimal or some other constraint, such as user defined linear and nonlinear constraints, may not be satisfied.

3.4.1 Pattern Search Applications

Pattern search has a wide range of applications to problems in which derivative based methods fail. Applications range from mechanical engineering to machine learning. A black box optimizer called Google Vizier is used to optimize hyperparameters of machine learning systems at Google (Golovin et al., 2017). Pattern search is one specific optimization method in the category of black box optimization.

3.5 Linear and Nonlinear Constraints

The specific Pattern Search optimizer used by Matlab is the Augmented Lagrangian Pattern Search (ALPS) whose goal is,

$$\min_{\mathbf{x}} F(\mathbf{x}) \tag{3.4}$$

subject to the nonlinear constraints $c_i(\mathbf{x}) \leq \mathbf{0}, \mathbf{i} = \mathbf{1}, ..., \mathbf{m}$ and linear constraints, (lower bound) $\leq$ $\mathbf{x} \leq$ (upper bound). Our nonlinear constraints arise from enforcing convexity and the linear constraints prevent vertices from overlapping or taking extreme values, such as allowing a vertex to lie far away from the rest.

Instead of directly minimizing the objective function $F(\mathbf{x})$ exclusively, Pattern Search sequentially minimizes the Lagrangian barrier function (Conn, Gould, and Toint, 1997),

$$\Theta(\mathbf{x}, \lambda, \mathbf{s}) = \mathbf{F}(\mathbf{x}) - \sum_{\mathbf{i=1}}^{\mathbf{m}} \lambda_{\mathbf{i}} \mathbf{s_i} \mathbf{log}(\mathbf{s_i} - \mathbf{c_i}(\mathbf{x})) \tag{3.5}$$

where components λ_i of the vector λ are non-negative Lagrange multiplier estimates and s_i of the vector $\mathbf{s}$ are non-negative shifts, and $c_i(\mathbf{x})$ are our nonlinear inequality constraints (Kolda, Lewis, and Torczon, 2006).

A constraint can be added to the problem using Lagrange multipliers. For example, to find $\min_x f(x)$ subject to the constraint that $g(x) = 0$, a Lagrangian multiplier function $L - \mathrm{f} - \lambda g$, can be incorporated and requiring that $\nabla f = 0$ and $\frac{dL}{d\lambda} = 0 \implies g = 0$. Pattern search implements nonlinear inequality constraints through use of a non-negative Lagrangian multiplier estimate λ in equation (3.5). The calculation of the Lagrangian multiplier estimates can be found in Conn, Gould, and Toint, 1991 and Conn, Gould, and Toint, 1997.

The initial Lagrangian multipliers λ_i are chosen by the algorithm and are decreased as the iterations proceed. Similarly the s_i values decrease proportionally to λ. Intuitively the reasoning behind decreasing λ and s_i as the algorithm progresses is to prevent the constraints from overpowering the minimization process. Initially it is important to enforce convexity, but as pattern search goes through more iterations, it should start approaching an optimum minimum value to the objective function, and avoid purely satisfying the constraints.

Section 2.4.2 of the computational framework above discusses how we implemented nonlinear convexity constraints in detail. Computationally we only implemented a single c which was able to encompass all the convexity constraints since it is either positive or negative based on convexity.

This means that if the concentrator is concave at any joint, the convexity constraint fails and is negative. c is only positive if the all the concentrator segments are aligned in convex manner. It is either positive or negative based on convexity.

Chapter 4

Concentrator Shape Optimization Results

Chapter 1 provided and overview of solar energy and introduction to solar thermal technologies. Then chapter 2 set up the computational framework and goals for a ray tracing architecture that determines the efficiency of a specified segmented solar concentrator design. Then in chapter 3 we discussed relevant optimization approaches.

In this chapter we will demonstrate the necessity for using gradient-free optimization techniques by showing objective function behavior, confirm pattern search effectiveness in finding optimal concentrator configurations, explain the efficiency and cost advantage of optimized segmented solar concentrators for low degree concentrators, and determine concentration configuration robustness for various designs.

4.1 Objective Function Behavior

To understand the nature of the objective function given in equation (2.1) and visually see the reasons gradient based solvers fail, we will investigate the nature of the objective function for a single interior movable vertex as shown in Figure 4.1. The vertices on either side of the aperture and receiver remain fixed while the y-coordinate of a single interior vertex is allowed to vary between the values of 1 to 6. The interior vertex has a fixed x-coordinate midway between the x-coordinates of the aperture and receiver.

Using 100 angles of Lambertian distribution originating from each of the 100 sources, for a total of 10,000 rays, the optical concentration ratio, or additive inverse of equation (2.1), of each concentrator configuration was recorded. The y-coordinate was varied between 10,000 evenly spaced values between 1 and 6. The resulting graph of the negative objective function versus the y-coordinate of the single moving vertex is shown in Figure 4.2.

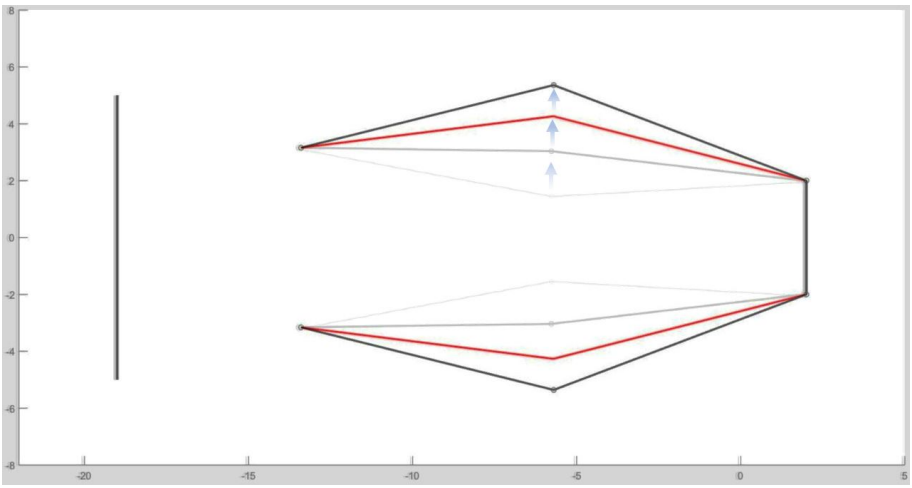

FIGURE 4.1: The above figure shows how the y-coordinate of a single joint is changed between the values of 1 to 6.

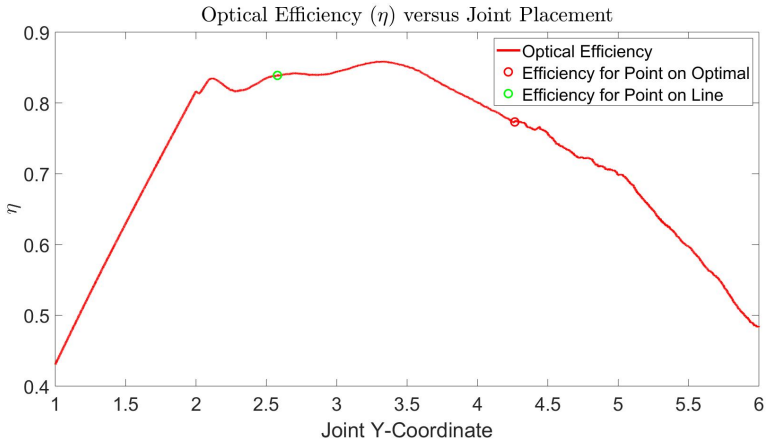

FIGURE 4.2: The above graph shows how the optical efficiency changes with the y-coordinate location of a single joint. Notice that neither the location of the y-coordinate corresponding to that of a linear receiver, nor that with the y-coordinate placed at the location along the ideal concentrator result in maximum optical efficiency. Furthermore, the graph has several local maxima/minima, making gradient based methods ineffective at finding the maximum.

The y-coordinate values corresponding to a linear concentrator is denoted by a green circle and the y-coordinate position of the vertex lying on the ideal concentrator is denoted by a red circle in Figure 4.2. Neither one of these gives a configuration that maximizes the percentage of rays reaching the receiver, but rather some intermediate y value between these

two configurations. Several local minima and maxima can be observed but overall the graph *appears* quite smooth in areas, such as around the green open circle denoting the location of the linear concentrator.

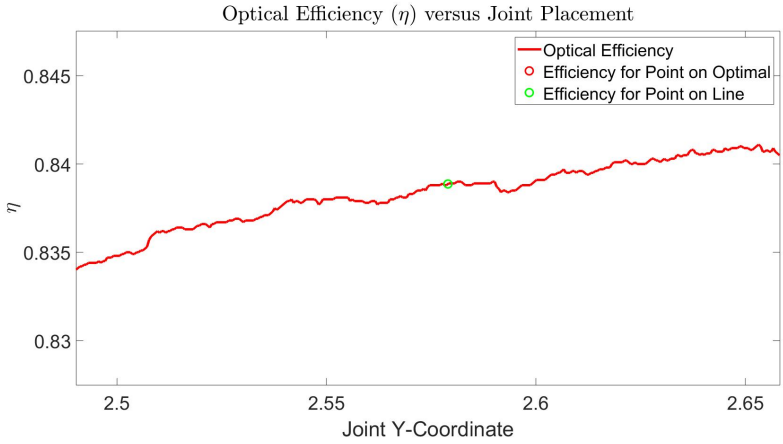

FIGURE 4.3: The above graph is a zoomed in version of the previous plot showing optical efficiency versus y-coordinate joint placement. Notice how even around the green circle denoting the location of the y-coordinate for a linear concentrator there are several local minima and maxima, making gradient based searches ineffective.

However, when zooming into Figure 4.2 in the seeming flat area around green circle of the linear concentrator, we see that the graph no longer looks smooth and several local minima and maxima become apparent, as shown in Figure 4.3.

Using an even finer mesh and zooming in even further around the green circle in Figure 4.2 we see that the graph is indeed locally flat almost everywhere, with abrupt jumps in the optical efficiency as shown in Figure 4.4. Larger local minima and maxima are shown in courser mesh plots, such as those in Figure 4.2, but even sections of the graph that previously appeared relatively smooth when viewed from this coarser mesh also demonstrate a plethora of local minima and maxima at the fine mesh scale of Figure 4.4. This fractal like nature of local minima and maxima at various scale levels, combined with the locally flat everywhere nature of the objective function make derivative-based solvers unsuccessful.

This fractal like behavior of local minima and maxima at different scales is also shown when increasing the dimensions of the problem. When both the x and y coordinates of the single vertex are allowed to vary as shown in Figure 4.5, irregular jumps in the objective function are similarly seen, as can be shown in the contour plot in Figure 4.7. Although the contour plot appears to indicate a smoothing for intermediate y-values between those on the linear concentrator line and the ideal concentrator configuration, a finer mesh reveals the same locally flat behavior with abrupt jumps is shown as that in Figure 4.4.

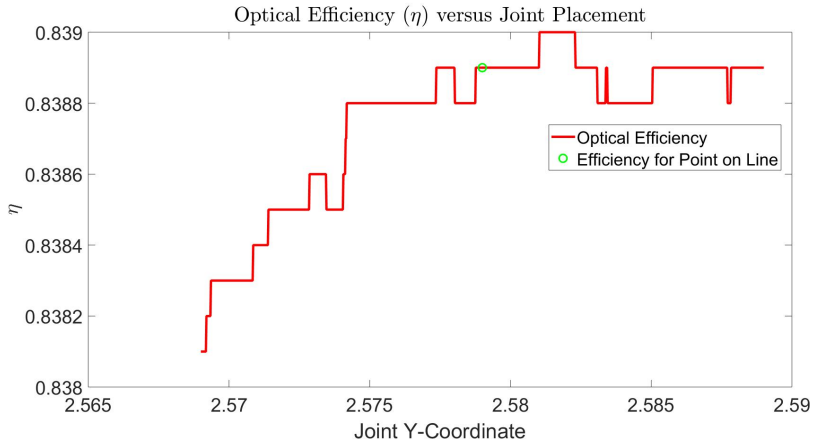

FIGURE 4.4: With a mesh of 0.00002 around the location of the y-coordinate for a linear concentrator, we see that the objective function is locally very flat, with sudden jumps in optical efficiency.

The contour plot appears smooth, but as discussed in Figure 4.4, at the microscopic level there is a fractal like structure that is rough with numerous discontinuities and undermines gradient based approaches. It is piecewise constant, which makes derivatives impossible to calculate.

4.2 Pattern Search Application

Given that the objective function is locally flat everywhere and that derivative-based optimizers would be ineffective, we decided to apply pattern search, a derivative free optimizer. The background, the advantages, and optimization method of pattern search are given in section 3.3.

In this section we will show how we validated the effectiveness of pattern search for this problem, selected appropriate algorithm parameters, and reduced the optimizer degrees of freedom for faster, better optimized results.

4.2.1 Parameter Selection

We assessed the effectiveness of pattern search in finding practical optimal solutions while manually adjusting a few parameters that we thought were of particular importance. In particular, we found that decreasing the initial mesh size and the mesh tolerance gave more accurate results in pattern search.

In addition, the maximum iterations were reduced to just 25 to prevent lengthy searches. We found that most of the time lengthy searches were due to the optimizer getting stuck

Parameter	Chosen Value
InitialMeshSize:	0.1
MaxIterations:	25
MeshContractionFactor:	0.5000
MeshExpansionFactor:	2
MeshTolerance:	$1.0000e^{-08}$

TABLE 4.1: The above table shows a subset of the Matlab pattern search parameters, some of which are default values and some of which are user defined. We varied these parameter values and assessed optimization performance. The values shown are the parameters that we found are effective for pattern search to reach appropriately optimum values.

in a bad design prevented the stopping criteria from being met or the convexity constraints from being satisfied.

We found that most of the other default values worked quite well. While the values that we found may not be absolutely ideal, we found them to be effective and sufficiently fast. Finding even better parameter values is an optimization problem in itself. There are a lot of degrees of freedom in selecting parameter values.

We were not able to utilize the vectorization feature of pattern search in Matlab. This was due the fact that our objection function itself is vectorized since we send in all rays into the concentrator at the same time. Utilizing the pattern search vectorization would require higher dimensional arrays to be implemented to deal with a matrix, rather than a vector, input into the ray tracer.

4.2.2 Degrees of Freedom Reduction

Pattern search is easily able to optimize the x and y coordinate location of a single vertex as, such as that depicted in Figure 4.5. As the number of vertices increases, the number of degrees of freedom to be optimized increases as well. Instead of increasing the degrees of freedom by 2 with each additional vertex, the x locations of each vertex can remain fixed while only allowing the y locations to be optimized, such as that depicted in Figure 4.1.

Reducing the number of degrees of freedom by fixing the x coordinate vertices for concentrators with larger numbers of vertices simplifies the optimization process and and prevents vertices from bunching together. Fixing x vertex coordinates was shown effective and often even produced better results than allowing x vertex movement. Allowing the x vertices to move sometimes leads to configurations in which vertices are optimized to locations very close to one other in the x direction.

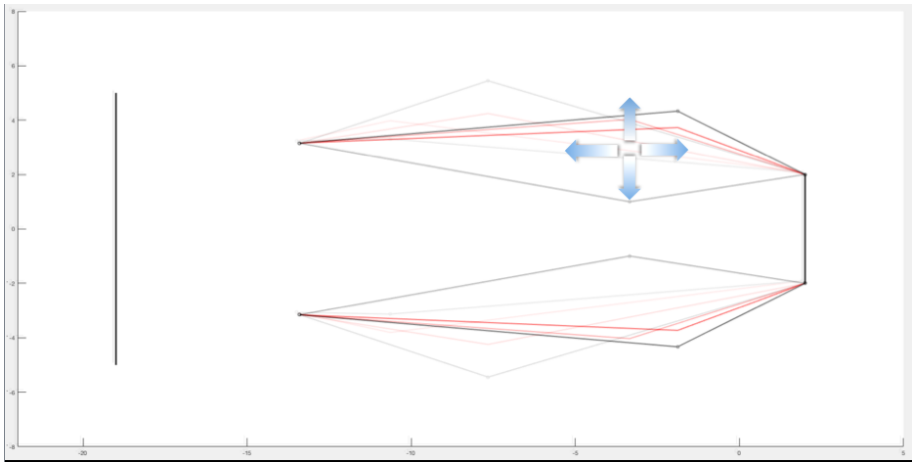

FIGURE 4.5: This figure shows how the coordinates of a single vertex can be varied in both the x and y directions.

4.2.3 Optimization Validation

We then allowed pattern search to optimize the location of a single vertex for a linear segmented solar concentrator of two segments, such as that in Figure 4.5. The optimized concentrator is shown in red in Figure 4.6.

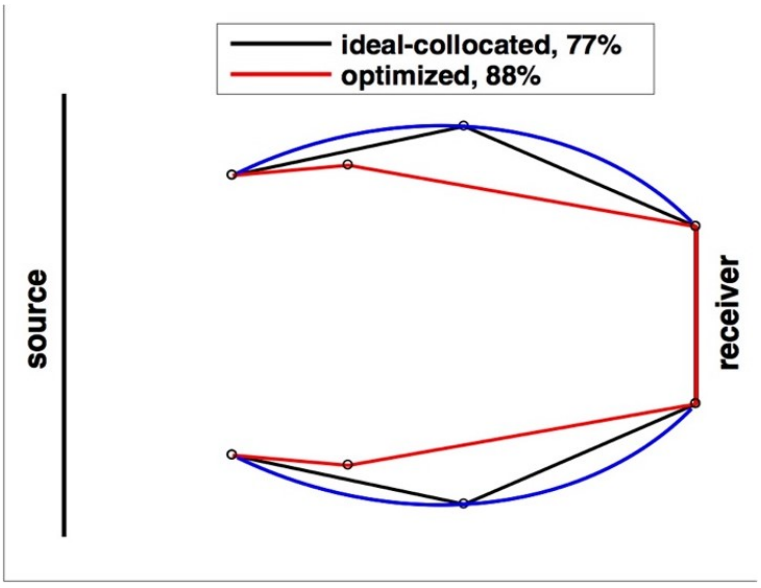

FIGURE 4.6: Efficiency Gain for Optimized Segmented Solar Concentrator

The configuration and efficiency obtained by the pattern search optimized concentrator is confirmed by the vertex location of highest efficiency found in Figure 4.7. This result validates that pattern search is working as expected and is able to find the most optimal concentrator configuration.

Again, note that the optimal location for the placement of a single vertex is at an intermediate point between a linear concentrator in two dimensions. This is similar to the result of a single vertex whose ideal location lies in between the green and red curves on the graph of Figure 4.2.

The high efficiency jump in joint location optimization indicates the need for the optimized placement of vertices for low degree linear segmented solar thermal concentrators. The optimal y-coordinate placement is not along that for ideal concentrator nor is the optimal x-coordinate equidistant between aperture and receiver.

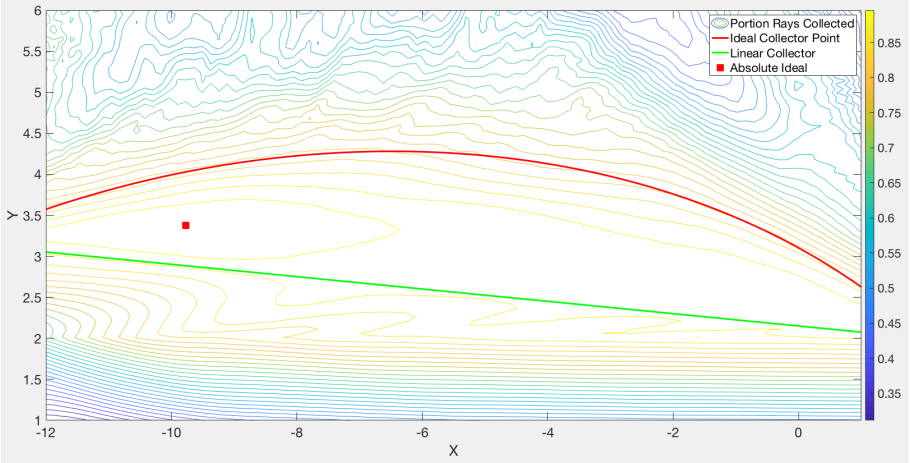

FIGURE 4.7: Contour plot showing the percentage of rays collected for a single vertex placed at given x and y coordinates.

4.3 Interior Angles Optimization

Instead of optimizing the joint vertex locations, it may be desirable to fix the overall concentrator length and optimize the interior angle of consecutive concentrator segments, as shown in Figure 2.2.

When the vertex location is optimized, the concentrator segment lengths are free to vary in length. When instead the interior angles of the concentrator are to be optimized, the lengths of each of the concentrator segments must be fixed. Such concentrator designs may be more favorable in manufacturing settings where concentrator wings must be made from a fixed length of reflective metal material and optimization is then used to determine the degree to which each joint must be bent for optimal efficiency.

However, it is not obvious how segment lengths should be chosen. As shown by the optimized concentrator in Figure 4.6, the two concentrator segments are not equal.

4.3.1 Segment Length Ratio Importance

Choosing the length of each concentrator segment length has an effect on the overall maximum optimal efficiency that may be obtained. Consider a concentrator with an overall fixed wing length $A + B$, such as that shown in Figure 4.8.

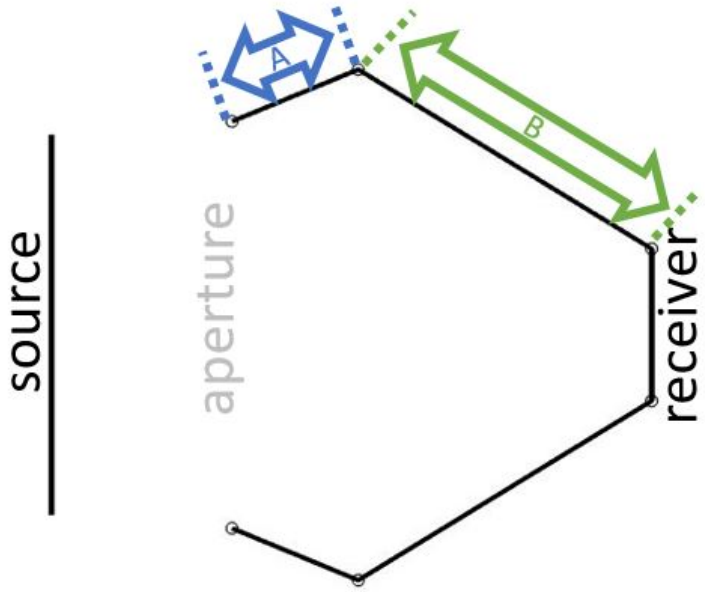

FIGURE 4.8: Diagram on the concentrator segment ratio lengths.

Allow the lengths of A and B to vary, or rather the ratio of $\frac{(\text{LENGTH OF A})}{(\text{LENGTH OF B})}$ is allowed to vary while the overall length $A + B$ remains fixed. The efficiency of the pattern search optimized configuration for each ratio of lengths is shown in Figure 4.9

4.4 Small Number of Segments Advantage

Figure 4.6 also shows the real advantage of optimized segmented solar concentrators is when there are just a few number of segments whose location is optimized. When a joint is simply chosen along the ideal equidistant from the aperture and receiver, as shown by the ideal-collocated configuration, such a concentrator configuration only performs at 77% efficiency. On the other hand, the optimized concentrator boasts an efficiency of 88%, an 11% efficiency gain.

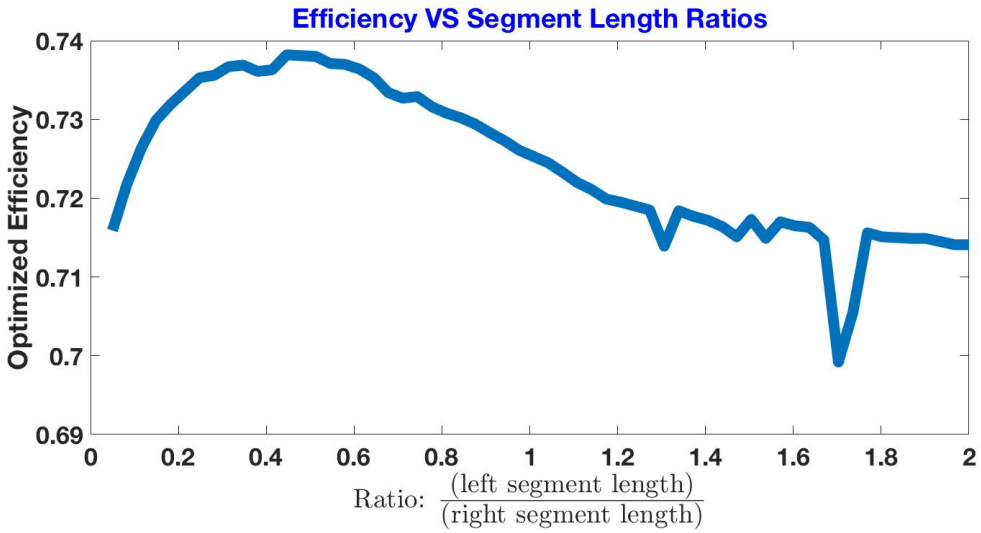

FIGURE 4.9: The above figure shows the effect of segment ratio lengths on the overall optimized concentrator efficiency.

The (x, y) vertex position of the two linear segmented optimized concentrator in Figure 4.6 is similar to the optimal vertex location found in Figure 4.7. Optimized segmented solar thermal concentrators show the most efficiency gain over their ideal-collocated counterparts when there are fewer segments.

When the number of segments is large, we see that the segmented solar thermal concentrator often approaches the shape of the ideal solar thermal concentrator with increasing efficiency. As the number of segments increases, the added increase from the optimization process becomes less significant. Hence, ideal-collocated and optimized segmented solar concentrators composed of a high number of linear segments on each wing do not show significant efficiency differences.

To display the optimization advantage, Figure 4.10 shows the difference in efficiency for an optimized concentrator of the specified number of segments versus a collocated ideal concentrator with an equivalent number of vertices. The plot was produced starting with a basic concentrator setup such as that in Figure 2.1 optimizing a single interior vertex.

There are a total of three vertices along each of the top and bottom concentrator wings corresponding to one on the aperture, an interior vertex, and on the receiver. The x value of the interior vertex is fixed half way between the x coordinate values of the aperture and receiver vertex values. The respective optimized and ideal collocated segmented concentrators are shown on the right with the respective efficiencies of each concentrator relative to the number of segments is shown on the left.

The largest different between the two curves in Figure 4.10 is for low numbers of segments with the greatest different being for a concentrator consisting of two segments. This shows

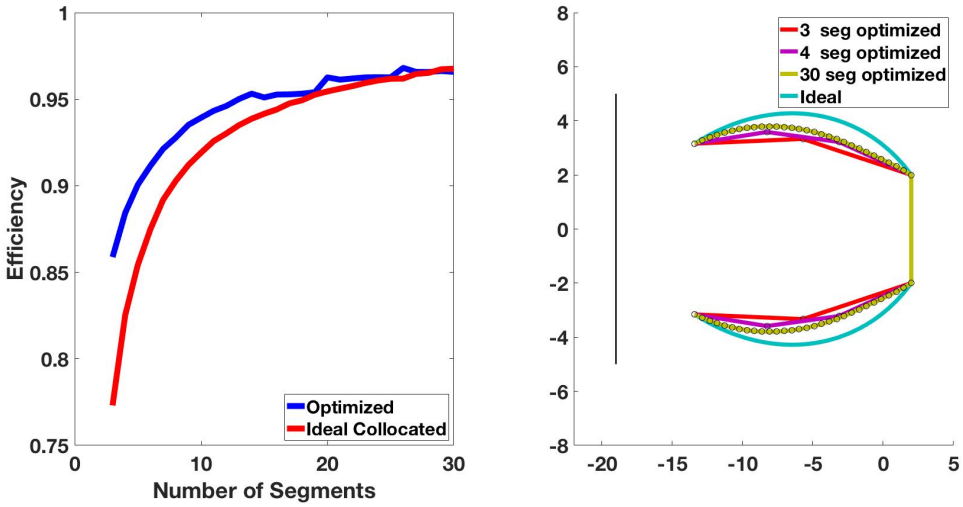

FIGURE 4.10: As the number of segments increases, the efficiency of the ideal-collocated segmented concentrator approximately equals the efficiency of an optimized segmented collocated linear concentrator. However, the optimized concentrators show much higher efficiency for low numbers of segments.

that concentrators consisting of a few number of segments show the most efficiency gains when optimized versus simply choosing discrete points along the ideal.

4.5 Sensitivity Analysis

Assessing the sensitivity of various concentrator configurations is very important to predict the performance of manufactured concentrators. Some analytical work has been done looking at the error in the concentrator slopes and its effect on acceptance angles (Winston et al., 2005). It is thought that nonimaging designs are more robust to manufacturing errors.

We take a computational approach instead of an analytical approach and directly quantifying efficiency losses with respect to manufacturing errors. We provide a systematic assessment of concentrator sensitivity under various degrees of manufacturing errors. This approach and level of theoretical sensitivity assessment which quantifies manufacturing error effects on device performance has not been done previously.

4.5.1 Sources of Concentrator Defects

In practice, concentrator segments would be manufactured and cut to specified lengths. However, there is inherent error in cutting and connecting concentrator segments. Segment length error would inevitably lead to a decrease in efficiency.

The degree to which error is tolerated depends partly on the number of segments the concentrator has. Clearly a concentrator with many segments, meaning many shorter segments, will require a machine with lower tolerance. Concentrators with only a few, longer segments can allow a higher error tolerance.

We define noise relative to the length scale of the segments by the following equation:

$$y_{\text{noise}} = (\text{length scale}) \times (\text{random normal[0,noise deviation]}) \tag{4.1}$$

where

$$(\text{length scale}) = \frac{(x_{\text{receiver top}} - x_{\text{aperture top}})}{(\text{number of segments on concentrator})} \tag{4.2}$$

and the noise deviation varies from 0 to .05 in .01 increments.

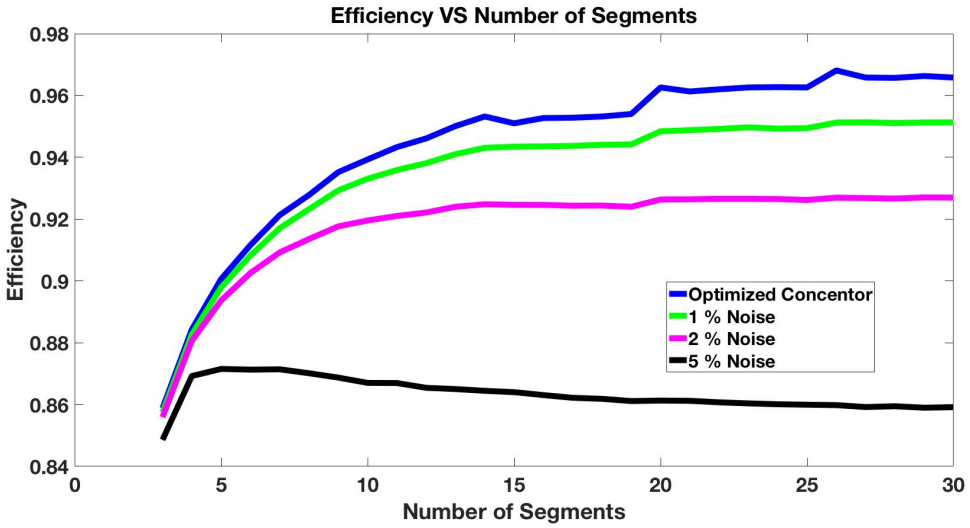

FIGURE 4.11: Inherent manufacturing errors lead to decreased efficiencies. The above figure shows how errors, modeled through adding noise to joint placement, compromise efficiency. Concentrators with large numbers of segments, and hence have a large number of joints, are more prone to large efficiency drops with too much noise since errors occur at each of the joint locations.

In Figure 4.11, we see that concentrator efficiency decreases with increasing levels of noise, as we would expect. However, there are particularly large drops in efficiency for concentrators with a large number of segments.

The reason the amount of error plays a larger role in efficiency for a large number of segments is likely due to the fact that error in each segment is contributing to the drop in performance. Concentrators with fewer segments have fewer sources of error to occur, even if deviation from the optimized location is larger.

Low degree concentrators are the most robust to noise errors. We see that the difference in performance for really low degree concentrators does not change much even when adding as much as 5% noise.

However, as the number of segments increases, noise levels become more important. Concentrators with a large number of segments, but also lots of noise show little to no improvement over concentrators with fewer numbers of segments. This is especially true for noise above 2%, after which device performance can actually decrease when adding more segments, such as is the case for 5% noise.

4.6 Speed Assessment

The ray tracer is vectorized in Matlab and optimization is highly efficient when paired with Matlab's built in pattern search function. No communication between various platforms is needed, increasing speed.

The output in Table 4.2 shows only 0.034882 seconds and 3 complete iterations and are needed to achieve a mesh tolerance of less than 10^{-8} when optimizing the y coordinate of a single vertex of the basic concentrator. Even when vertices are increased according to that described in section 2.3.2, pattern search still only requires seconds to optimize 28 interior vertices.

```
                                    Max
  Iter   Func-count       f(x)      Constraint   MeshSize      Method
    0         1      -0.8389          0.5          0.1
    1         7       -0.857            0        0.001   Increase penalty
    2        29      -0.8582            0    9.333e-07   Update multipliers
    3        71      -0.8588            0     8.71e-10   Update multipliers
Optimization terminated: mesh size less than options.MeshTolerance
 and constraint violation is less than options.ConstraintTolerance.
Elapsed time is 0.030852 seconds.
```

TABLE 4.2: The above display shows the Matlab console output when optimizing the y coordinate of a single vertex of the basic concentrator.

Typically less than 7 iterations are required by pattern search to reach an optimum within a tolerance of 10^{-8} with a run time of seconds. The mesh size decreases approximately by a power of 10 with each displayed iteration. Since we have a nonlinear constrained problem, the method column either displays 'Increase penalty', or 'Update multipliers', which refers to changes implemented on the Lagrangian multipliers by the pattern search optimizer.

The maximum constraint column displays a positive value of 0.5 if the constraints are not satisfied and 0 if the constraints are satisfied. The constraint is initially not satisfied since the initial vertex lies on a linear concentrator wing, which is not convex. The column $f(x)$ refers to the value of the objective function.

Chapter 5

Conclusions

Although ideal 2D CEC designs exist, the performance of these designs quickly changes when the concentrator is approximated by segmented collocated linear segments. We aim to remove the limitations of continuously varying shapes and 2D designs by taking a computational approach.

5.1 Achievements and Results of Method

Our computational approach includes optimizing segmented solar concentrator efficiency for a given number of segments. The result is a design that is relatively easy to manufacture, while maximizing efficiency for the given design constraints. As outlined in 2.1, the primary goal was to present an optimization method and resulting concentrator configurations that are:

- Easy to manufacture
- Adaptable to different user designed configuration criteria and constraints
- Highly efficient, optimal, and practical
- Computationally fast
- Robust to slight changes caused by error

Our method addresses all of these goals. In addition, our method can be used to design low degree efficient concentrator designs which have not been discussed in other literature.

5.1.1 Easy to Manufacture

One primary goal achieved was designing a concentrator that can be manufactured cheaper while minimally sacrificing on concentrator efficiency. We call such concentrators to be optimal. They are no longer ideal in terms of collecting every ray that enters the aperture, but they give the highest optical concentration ratio efficiency for the given design parameters.

There are several factors which make may make linear segmented concentrators easier and cheaper to manufacture, which include:

- Linear segments instead of curved surfaces
- Efficient low degree concentrators
- Symmetric
- Definable concentrator wing lengths
- Definable aperture size
- Definable absorber shape

5.1.2 Optimized by a computationally fast approach

We have shown that our method gives theoretically efficient designs and results in practical configurations in seconds. Our vectorized ray tracing method in Matlab combined with Matlab's built in pattern search optimization give results in seconds. If one were to use multiple softwares for the ray tracing and optimization, there would be a huge communication lag between various softwares. We implement everything in Matlab and our method is also not proprietary.

Our optimizer allows the user the adaptability to choose the number of vertices while optimizing at each step. The number of vertices to be increased incrementally, optimizing at each step, until the desired number of vertices is reached.

Hence, the optimizer used to determine the optimal concentrator configuration is fast and also gives good results. This is make possible by using:

- Vectorized ray tracer
- Single software for both ray tracer and optimizer to reduce communication lag between various softwares
- Any number of segments on reflector

5.1.3 Adaptable to Various Design Criteria

Our method also allows lots of user flexibility to specify design criteria. Some user specified parameters include the number of segments, optimization preferences such as interior angle or vertex location optimization, and ray configuration. Hence, users can optimize a configuration that fits their needs.

Users may also choose trough or basic concentrator configurations. These two configurations optimize different aspects of the concentrator configuration: joint coordinate values

or interior angles between consecutive segments. Optimizing the angles between consecutive segments while keeping segment lengths fixed seems to be a more realistic portrayal of the manufacturing process. However, optimizing interior angles moves the location of the aperture.

Setups which require specific aperture sizes or the ability to increase the number of segments may prefer joint coordinate optimization. Configurations with larger numbers of segments were also less dependent on the initial configuration if segments were incrementally increased with coordinate join locations were optimized. Both approaches lead to comparably efficient designs overall.

Therefore, we addressed the fact that concentrator designs are adaptable to various design parameters such as:

- Any absorber shape
- Select fixed wing lengths or maximum concentrator width/length
- Select a maximum or fixed aperture size

5.1.4 Robust to manufacturing errors

The new low degree designs that we were able to find with our optimization method displayed:

- Robust to slight changes, especially for low segmented designs
- Limited efficiency losses from small design errors
- Limited efficiency loss due to inherent manufacturing errors

5.1.5 Highly efficient, Optimal, and Practical

We were also able to show that pattern search is able to find the most optimal configuration when optimizing over two degrees of freedom. Our method is also able to effectively find optimal designs for higher degrees of freedom, with concentrator efficiency above segmented ideal concentrators. We also enforce convexity, preventing the optimizer from becoming stuck in impractical, non-convex configurations.

Optimized low segmented designs are also shown to result in the highest efficiency gains compared to a segmented concentrator of collocated points along the ideal. Therefore, we were able to show that our method results in:

- Optimized concentrator configurations under given constraints
- At least or more efficient than collocated segmented ideal concentrators

- Optimized low segmented designs show the highest efficiency gains compared to collocated points along the ideal
- Convexity can be enforced on the reflector shape

Overall, we showed that our method is not only fast, but is shown to be effective in finding optimal designs specifically for low degree optimization problems. This is important since these configurations are of most interest from a manufacturing, robustness, and efficiency gains, as mentioned.

5.2 Limitations

This method is shown to give optimal designs specifically for low degree optimization problems. The optimization process becomes less effective for large degree problems since the optimization becomes more difficult.

When given a larger number of variables to optimize, pattern search also becomes more dependent on the prior, or the initial configuration of the concentrator. This is partially due to convexity constraints that prevent such configurations. Hence, several joints are required to move at once in the same direction to preserve convexity while moving substantially from their initial locations. However, when convexity is not required, we found that pattern search often finds a concave design and then is unable to correct itself and move back to a convex design, causing the optimizer to become stuck in less optimal configurations.

Lower degree optimizations were also shown to be more robust to errors. Concentrators consisting of fewer numbers of segments were more robust to manufacturing errors. Concentrators with higher numbers of segments showed more error propagation and an overall substantial decrease in efficiency.

Overall our optimization method lends itself best to lower degree optimization problems, which show more promising results in terms of optimizability, robustness, and manufacturing advantage.

Part II

Luminescent Solar Concentrators

Chapter 6

Background on Solar Electric and Luminescent Solar Concentrators

Section 1.1 talked about the two main forms of solar energy, solar electric and solar thermal, and how they compliment each other in terms of uses and storage abilities. In this part we will focus on solar electric energy and concentrators that may be used in tandem with photovoltaic (PV) devices, specifically luminescent solar concentrators (LSCs).

6.1 Solar Photovoltaics (PVs)

Solar photovoltaics, commonly referred to as PVs, employ the photovolatic effect to create electricity. PVs are most commonly comprised of silicon. PVs create electron flow through the implementation of a P-N junction, which creates a field, or a space charge region. The structure of a P-N junction used to create a photovoltaic cell is shown in Figure 6.1.

6.1.1 Formation of the P-N Junction

While the bulk of the cell is made up of silicon, a few other atoms are inserted into the silicon crystalline structure, a process called doping. These impurities are added in specific way to the upper and lower layers of a cell in order to create the space charge region at the junction between these two layers.

In the upper layer, atoms with an extra valence electron with respect to silicon, such as phosphorus or arsenic, is doped into the silicon crystalline structure (Laube, 2019). Pure silicon binds into a diamond cubic lattice formation. The rigid silicon crystalline structure binds to the minute quantities of group V dopant, such as phosphorus, in the same lattice structure, but this creates an excess negative charge of this region (Honsberg and Bowden, 2019).

The overall negative charge of the upper region are the reason that the upper layer is commonly referred to as the N layer. The dopant impurities add extra unbound electrons to the crystal, meaning the region has an excess of electrons.

The lower layer is doped with atoms with one less valence electron with respect to silicon, such as boron, aluminum or indium (Laube, 2019). The minute quantities of these group III

impurities are similarly bound into the diamond cubic lattice formation of the bulk silicon material, creating an overall positive charge in this region (Honsberg and Bowden, 2019).

The lower layer is often referred to as the P layer due to its overall positive charge. The dopant atoms have one fewer electron for binding, meaning that the crystalline structure is missing a binding electron to create the diamond cubic lattice structure at the location sites of these dopants. This creates a region of excess positive charge that needs electrons to properly bind.

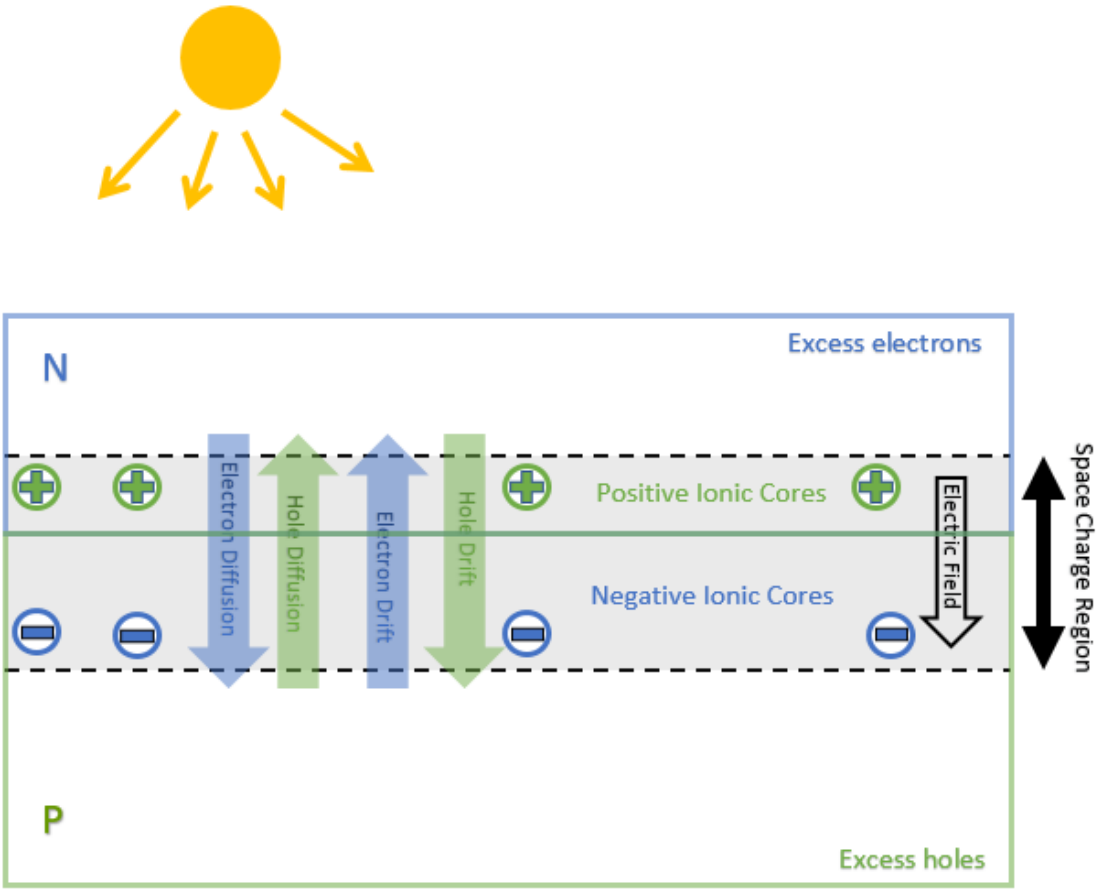

FIGURE 6.1: This figure shows how a P-N junction is used to create a field, or space charge region, at the interface of these two layers. When solar radiation excites electrons near the surface of the photovoltaic cell, electrons are pushed are pushed upwards by the field. The excess of electrons in the upper N region pushes electrons through an outer circuit back towards the lower P region, creating a current.

6.1.2 Space Charge Region

Since the lower layer is in need of electrons to stabilize the diamond cubic lattice structure in which the atoms are held, excess electrons from the upper layer flow across the interface between the two. This flow of electrons away from the N layer near the intersection of the P-N layers exposes the positive ionic cores of the group V elements within the lattice. The positive ionic cores result from the additional proton in the nucleus of the group V elements compared to silicon.

Similarly, as the excess negative electrons from the N region flow into the P region, negative ionic cores are created at the locations of the group III impurities. This is due to the fact that the group III elements have one fewer proton in their nucleus than silicon.

The positive ionic cores in the upper region and the negative ionic cores in the bottom layer exposed near the interface due to this electron movement creates an electronic field, as shown in Figure 6.1. This region on either side of the interface between the two layers is referred to as the space charge region.

6.1.3 PV Electricity Generation

The top N layer is typically made as thin as possible. This is so that solar radiation passes through the N layer and excites an electron in the space charge region. This excited electron is pulled due to the electric field in this region and moves upward.

As the electron enters the N region, this region already has an excess of electrons, creating the push of electrons needed to pass through an external load. This movement of electrons generates a current, and thereby generate electricity from the photovoltaic effect.

6.1.4 Cost and Efficiency

Solar photovoltaics are effective in generating electricity from the sun. However, production of photovoltaics can be expensive. Silicon PV cells must be carefully doped and crystallized to preserve the diamond cubic lattice. Furthermore, the silicon used in the PV must be very pure, contributing processing costs.

In addition, only certain wavelengths of sunlight are able to excite electrons in the silicon lattice to create a current. This means that only a portion of sun's radiation is turned into electricity. Wavelengths above or below the band gap are lost by either passing through or generate heat within the PV, further decreasing the efficiency of the PV. PVs more efficiently convert longer wavelengths into electricity.

Some things added to silicon PVs to increase efficiency include multi-junction tandem PVs and luminescent solar concentrators. Multi-junction PVs are made with different semiconductor materials in addition to silicon and include several P-N junctions. The additional P-N junctions increase the amount of sunlight converted into electricity since each junction has a different band-gap, or wavelength range which is converted into a current.

6.2 Luminescent Solar Concentrators (LSCs)

Luminescent solar concentrators emerged in the 1970's as a way to boost solar cell efficiencies by concentrating solar solar radiation onto them (Debije and Verbunt, 2012). Luminescent solar concentrators increase the electricity output of a PV cell by concentrating more sunlight within the bandgap onto the PV than would otherwise strike the PV if faced directly towards the sun.

The concentrating effect is due to the dimensional and material properties of LSCs. As shown in Figure 6.2, the lateral top surface is larger than the edge areas, meaning the photon density incident on the top surface is significantly larger than it would be on photovoltaic at the edge if it directly faced the sun. Directing these extra photons onto the PV at the edges creates the concentrator effect.

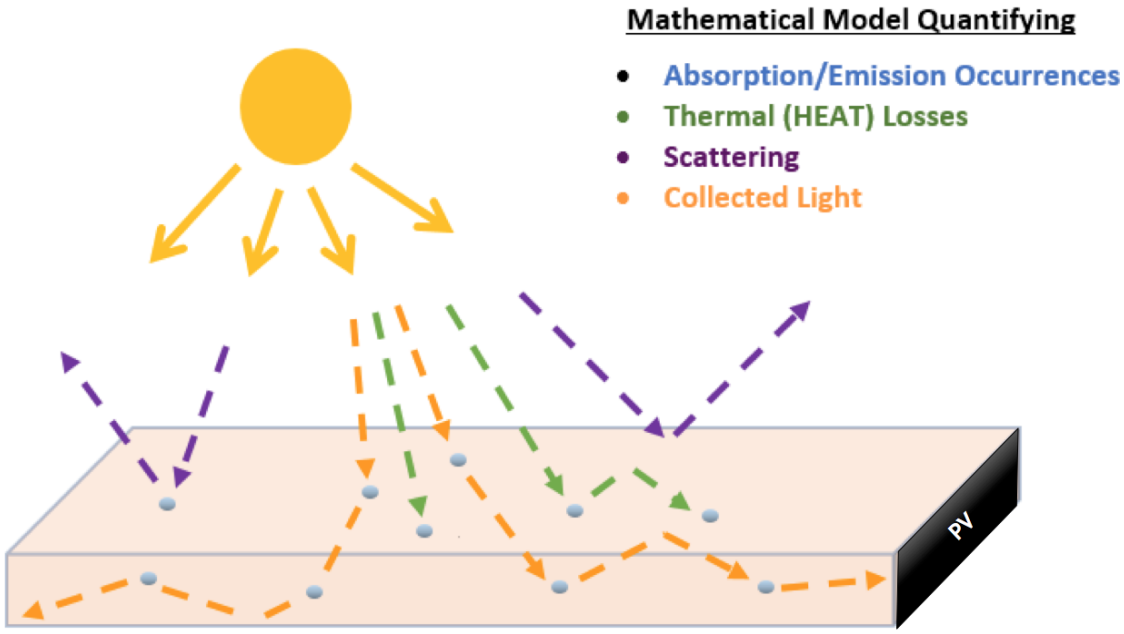

FIGURE 6.2: This figure shows a luminescent solar concentrator and the various outcomes to sunlight entering through the top. Sunlight is either reflected back through the top surface due to scattering, lost within the LSC due to thermal heat losses, or collected at the PV on the edge.

The concentration factor is the ratio between incoming irradiance on the LSC top surface and the irradiance that ends up at the edge of the LSC, where the PV is located (Rooij, 2019). This can be written as,

$$C_{LSC} = \frac{(\text{irradiance on top surface in } \frac{kW}{m^2})}{(\text{irradiance at LSC edge in } \frac{kW}{m^2})} \tag{6.1}$$

Instead of the concentration factor, we determine LSCs performance in terms of efficiency, defined as the ratio of incoming radiant flux on the top surface to that at the LSC edge. Incoming light is modeled as photons, meaning efficiency can be written as the following percentage,

$$E_{LSC} = \frac{\text{(number of photons entering top surface)}}{\text{(number of photons reaching PV at edge)}} \times 100\% \tag{6.2}$$

LSCs are typically made of a polymeric or glass waveguide with luminescent molecules (Debije and Verbunt, 2012). Ideally luminescent molecules should have a broad absorption spectrum, but also have a large Stokes shift to minimize self-absorption. The luminescent molecules should also have a large quantum yield so that absorbed radiation is again emitted as a photon of light and not lost.

Light enters through the top of the LSC. The bottom of the LSC is a mirror to double the absorbing path length for incident radiation (Weber and Lambe, 1976). Entering light must be absorbed by the luminescent material of the LSC within this distance or else it is lost back through the top surface. Light lost through the top surface is considered scattered.

Light absorbed by the luminescent LSC material is then emitted as a photon of light or lost due to self-absorption. The amount of absorbed light emitted by the luminescent material depends on the quantum yield. Materials with high quantum yields, meaning a large percentage of the absorbed light is emitted again as light, make the best LSCs.

The energy of absorbed light that is not emitted as another photon of light is lost to self-absorption. This is commonly referred to as self-absorption losses. Although not a completely accurate description, we will call this light to be lost to thermal or heat losses. These losses may occur due to lattice vibrations.

Ideally, emitted light is guided through internal reflections to the edge of the LSC, incident on the PV. Light may undergo several absorption and emission events before reaching the edge. The light that lands at an edge surface is referred to as collected light.

Ideally the extra concentration of photons onto the PV should more than compensate for the added cost of attaching the LSC, overall reducing the cost of the solar electricity. LSCs have not been applied commercially because they have not yet shown to be cost effective even though panels of glass or polymer are far less expensive than the equivalent size solar panel (Sholin, Olson, and Carter, 2007).

There have been several different studies of LSCs using different fluorescent dyes and semiconductor quantum dots. Fluorescent generally have narrower absorption bands (Van Sark et al., 2008) which limit LSC efficiency.

Since then quantum dots have been studied as luminescent particles for LSCs due to their broader absorption spectrum. One drawback of most commonly used quantum dots is that they emit in the visible region of the spectrum (Coropceanu and Bawendi, 2014), though there have been quantum dots that better match the band gap of silicon. However, quantum dot LSCs oxidize and degrade over time (Meinardi et al., 2015).

6.3 Perovskite as LSC's

Perovskite, as used in solar technologies, consists of a methylammonium ion ($CH_3NH_3^+$) surrounded by an octahedron of anions which also bond to lead (Pb) in a cubic crystalline structure (Green, Ho-Baillie, and Snaith, 2014). The anion is a halogen ion which is typically iodine (I), chlorine (Cl), bromine (B), or acetate (CH_3COO^-).

Interest in perovskite has recently exploded due to its high efficiencies and low cost. Perovskite solar cells were derived from dye-sensitized solar cells. The liquid-based dye-sensitized methylammonium lead halide perovskite on nanocrystalline TiO_2 surface was shown to produce a photocurrent first in 2009 (Park, 2015).

The 3-4% power conversion efficiency reached efficiencies above 20% in just a few years, making it the fastest advancing solar technology in history. The current record perovskite solar cell efficiencies lies at 25.2% (NREL, 2019). However, perovskite suffers from structural instabilities that cause deterioration when exposed to humidity (Yang et al., 2015).

The recent growth in prominence of perovskite in the solar field motivated us to consider the possibility to use them as LSCs due to their photoluminescent properties. Perovskite has a broad absorption band, high quantum yields reaching up to 80% (Leijtens et al., 2015) and a high refractive index of 2.5. The high refractive index increases the likelihood of total internal reflection, decreasing the amount of photons lost back through the top surface.

In addition, perovskite is easily manufactured as thin films. These thin films can be placed in areas where PVs is not possible since LSCs can also collect diffuse light. These properties make perovskites good candidates for LSCs and may boost efficiencies enough to make manufacturing cost effective.

Chapter 7

Monte Carlo Framework

7.1 Introduction

This chapter will present a Monte Carlo (MC) computational framework for luminescent solar concentrators (LSCs), extending the work done by Sahin, Ilan, and Kelley, 2011 in the paper "Monte-Carlo simulations of light propagation in luminescent solar concentrators based on semiconductor nanoparticles". We provide modifications to previous Monte-Carlo simulations that improve flexibility and decrease computation time. We then extend this improved Monte-Carlo technique to perovskite LSCs to gain deeper insight on the viability of perovskite LSCs and determine the most ideal composition and thickness for such a device.

We will describe the steps of our photon tracking Monte Carlo simulation in detail. This includes the use of the Beer-Lambert Law to determine absorption distances and emission wavelengths and Fresnel and Snell Law conditions imposed on the boundary.

7.2 Monte Carlo Simulation Framework

Monte Carlo (MC) is a ray tracing technique that is a common tool used to simulate photon transport (Jacques and Wang, 1995). Our Monte Carlo simulation accounts for radiation losses through the top surface (from Fresnel equations) and losses due to photons not being absorbed (based on Beer-Lambert law) or not emitted (based on quantum yield).

In this way, a photon trajectory is followed until it either:

- escapes back through the top surface
- reaches the photovoltaic (PV) cell
- is lost due to radiation effects (i.e. not emitted, and lost due to self-absorption)

Ideally a photon is absorbed and emitted exactly once before reaching the PV cell. With multiple absorption occurrences, the chance of the photon reaching the PV cell decreases due to the quantum yield. The quantum yield is the ratio of emitted photons to absorbed photons. In other words, it is the probability that an absorbed photon is emitted.

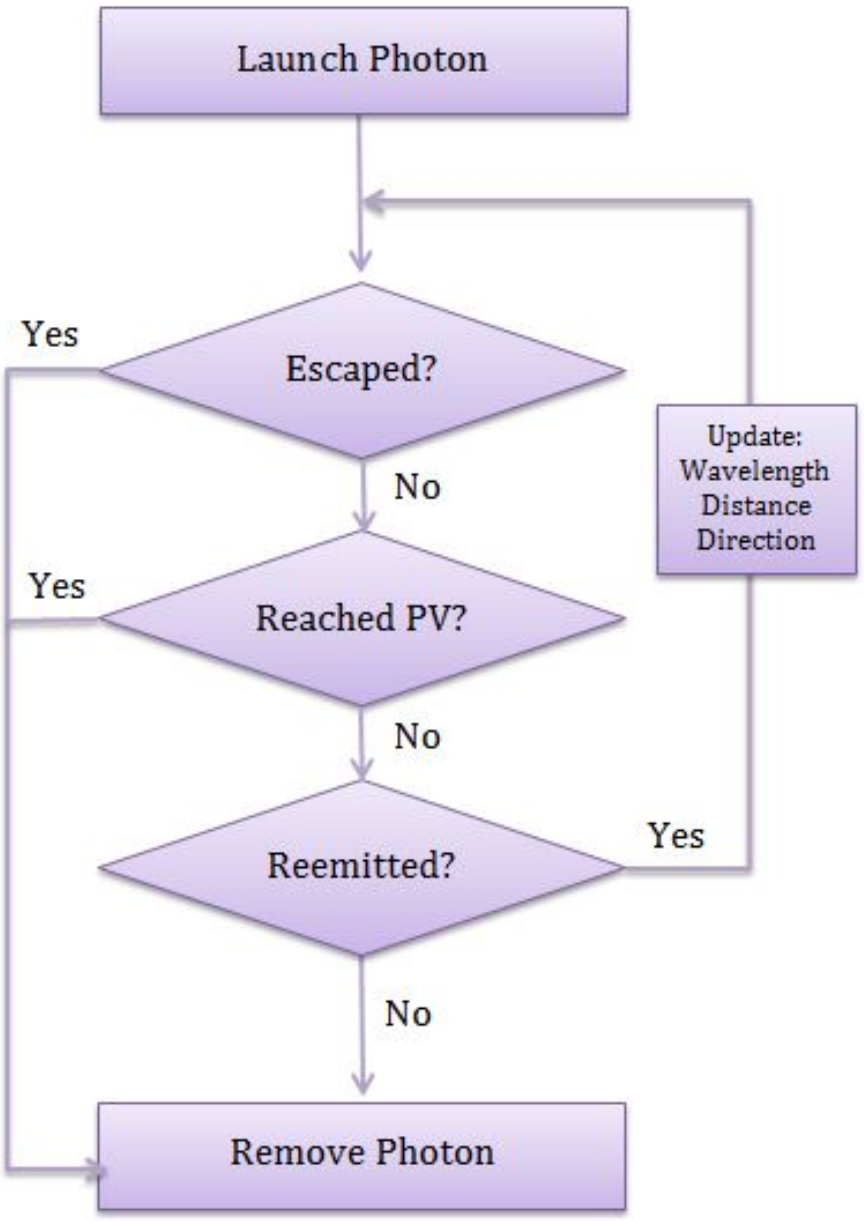

FIGURE 7.1: This figure shows the computational path of a photon through a luminescent solar concentrator.

The computational path followed by a photon in our Monte Carlo method is shown in Figure 7.1.

7.2.1 Propagation Distance

As shown in the Monte Carlo photon tracking scheme in Figure 7.1, initially a photon is launched into the LSC. A photon is launched with the following values:

- initial position (x, y, z)
- initial angle $\phi_0 \in [0, \pi]$ with respect to the normal to the top surface
- angle $\theta_0 \in [0, 2\pi)$ in the plane parallel to the top surface

Typically, we choose $\phi_0 = 0$, denoting a photon entering the LSC normal to the top surface. The photon also carries with it an initial wavelength λ_0, which is sampled randomly from the normalized solar spectrum provided by NREL (Emery, 2000).

The photon then travels a propagation distance of Δs before being absorbed, as determined by the Beer-Lambert law discussed in the next section. Before the photon is absorbed at the propagation distance, Δs, the photon may hit the walls of the LSC. The bottom surface is assumed to be a perfect mirror, and reflects the photon in accordance to Snell's law.

7.2.2 Probability of Escape

However, if the photon hits the LSC top surface (i.e. the LSC-air boundary), it can be either reflected or transmitted. A photon that is transmitted through the LSC top surface is said to be “escaped". The Fresnel equations to provide a “probability" that the photon will be reflected each time it reaches the top surface. The Fresnel equations are described in more detail later in this paper.

Since statistically reliable results for the MC simulation are reached after approximately 10^5 photons are launched into the LSC (Sahin, Ilan, and Kelley, 2011), the amount of photons reflected and transmitted through the top surface using the Fresnel coefficients as a probability approach the portion of light that would be transmitted and reflected respectively at the LSC top surface interface.

7.2.3 Collection

If the photon did not escape through the top surface over it's propagation distance, the Monte Carlo simulation then checks whether the photon reached a PV cell. PV cells are assumed to be on all four sides of the LSC. Therefore, any photon that reaches a side wall of the LSC is assumed to be “collected" by the PV.

7.2.4 Emission Probability

If the photon neither escapes from the LSC nor is collected by the PV over the propagation distance Δs, the photon is assumed to be absorbed by the LSC. The probability that the

photon is then emitted is determined by the quantum yield. Photons that either escaped from the LSC, reached the PV or were not emitted are respectively tagged and removed from the MC simulation.

If the photon is emitted, the current position of the photon (x, y, z) is updated. It is also assigned an updated wavelength sampled randomly from the normalized emission spectrum of the LSC material and an updated direction, as determined by updated angles ϕ and θ. These angles are assigned assuming isotropic emission, meaning there is an equal probability that the photon is emitted in any spacial direction.

7.3 Absorption

The probability of a photon of wavelength λ being absorbed after a propagation distance of Δs (in meters) is given by the Beer-Lambert Law (Sahin, Ilan, and Kelley, 2011),

$$p(\Delta s; \lambda) = 1 - 10^{-\epsilon(\lambda) M \Delta s} \tag{7.1}$$

where M is the molar concentration of particles (mol/L), and $\epsilon(\lambda)$ is the extinction coefficient ($L/mol\ cm$).

Assuming that $\xi = 1 - p(\Delta s; \lambda)$ is a uniformly distributed random variable in $[0, 1]$, we can invert equation (7.1) to obtain the propagation distance,

$$\Delta s = -\frac{1}{\epsilon(\lambda) M} \log_{10} \xi \tag{7.2}$$

The extinction coefficient $\epsilon(\lambda)$ is determined by the absorption spectrum, which is shown by the blue curve in Figure 7.2 below. Since photons with a wavelength near 300nm are more readily absorbed by perovskites, the extinction coefficient will be higher and hence the propagation distance will be shorter.

Perovskites do not readily absorb photons of wavelengths above 800nm, meaning that the extinction coefficient $\epsilon(\lambda)$ for wavelength values in this range will be much smaller. Hence, the propagation distance distance for photons of higher wavelength will be much longer since they will go a further distance before being absorbed.

The perovskite reemission spectrum is shown by the red curve in Figure 7.2 (Nikolaidou et al., 2016). Notice that the emission spectrum lies primarily in a wavelength range where the perovskite does not readily absorb. Hence, emitted photons are unlikely to be reabsorbed. This is ideal, since optimally photons are absorbed and emitted exactly once to prevent losses due to the quantum yield.

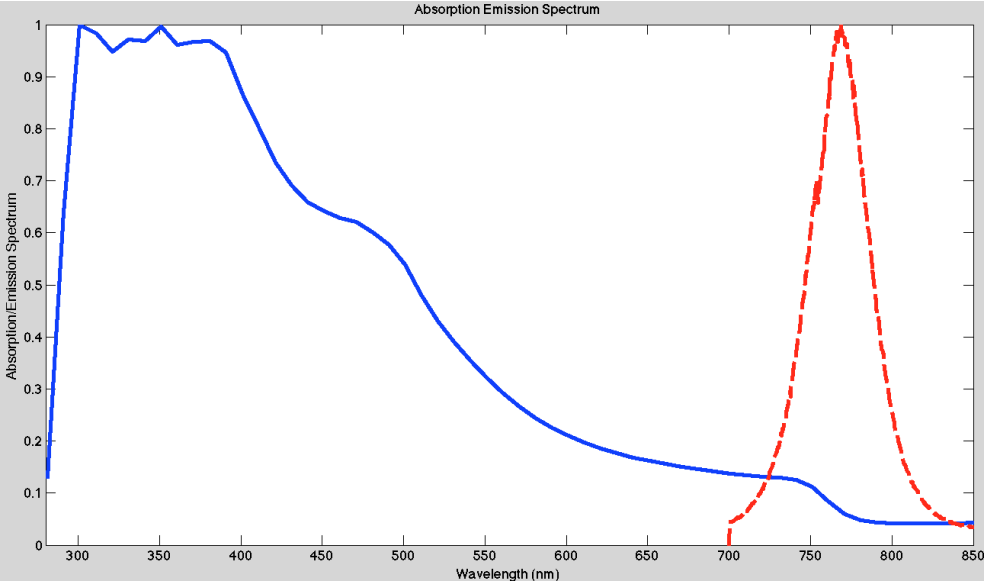

FIGURE 7.2: Absorption and Emission Spectra for Perovskites

7.4 Top Surface Reflection/Transmission

Since sunlight is unpolarized, the light inside the LSC is assumed to also be unpolarized. Hence, the Fresnel reflection coefficient for light incident on the LSC-air interface at an angle ϕ with respect to the normal is given by,

$$R(\phi) = \frac{1}{2}R_{\parallel}(\phi) + \frac{1}{2}R_{\perp}(\phi) \tag{7.3}$$

This can also be written as,

$$R(\phi) = \frac{1}{2}\left(\frac{n_p\sqrt{1-n_p^2\sin(\phi)^2} - |\cos(\phi)|}{n_p\sqrt{1-n_p^2\sin(\phi)^2} + |\cos(\phi)|}\right)^2 + \frac{1}{2}\left(\frac{n_p|\cos(\phi)| - \sqrt{1-n_p^2\sin(\phi)^2}}{n_p|\cos(\phi)| + \sqrt{1-n_p^2\sin(\phi)^2}}\right)^2 \tag{7.4}$$

where n_p is the refractive index of perovskites.

The reflection coefficient $R(\phi)$ is used as the probability that a photon striking the top surface at an angle ϕ with respect to the normal is reflected. Hence, the transmission coefficient, $T(\phi) = 1 - R(\phi)$, is the probability that the photon is transmitted, or "escapes" from the LSC.

7.5 Emission

Photons absorbed by perovskite material are emitted only if $\xi <$ (quantum yield of perovskites), where ξ is randomly generated from a uniform distribution on $[0, 1]$. Emitted photons are isotropically distributed with updated values of $\theta \in [0, 2\pi)$ and $\phi \in (0, pi)$ defined by:

$$\theta = 2\pi\xi \tag{7.5}$$
$$\phi = \arccos(2\xi - 1) \tag{7.6}$$

Where each ξ is a unique randomly generated variable from a uniform distribution on $[0, 1]$.

The wavelength of the photon is also updated by randomly sampling from the normalized emission spectrum. In this way, the luminescence is said to be "memoryless" (Sahin, Ilan, and Kelley, 2011), meaning that the wavelength of the emitted photon is based solely on the emission spectrum of perovskite and is independent of the wavelength of the photon prior to absorption.

The photon is then assigned a new propagation distance, Δs according to equation (7.2) with a newly chosen random variable ξ. The photon is then tracked again from it's current position (x, y, z), to it's new position (x', y', z') defined by,

$$x' = x + \Delta s(\sin(\phi)\cos(\theta)) \tag{7.7}$$
$$y' = y + \Delta s(\sin(\phi)\sin(\theta)) \tag{7.8}$$
$$z' = z + \Delta s(\cos(\phi)) \tag{7.9}$$

The process described above is repeated, as shown in Figure 7.1, until the photon either:

- Reaches PV cell
- Escapes from the LSC
- Gets lost due to radiation effects

7.6 Optical Efficiency

The solar-averaged optical efficiency $\overline{\eta}$ is the ratio of incident photons with solar-spectrum averaged wavelengths λ to collected photons. Since the initial photon wavelengths in our Monte Carlo simulation are sampled from a normalized solar spectrum, the solar-averaged optical efficiency $\overline{\eta}$ is just the ratio of collected photons to incident photons. The number of incident photons is the total number of photons used in the MC simulation.

One important role of MC simulations is to compute optimal LSC parameters. The usefulness of an LSC is often measured by LSC gain $\overline{\Gamma}$, where

$$\overline{\Gamma} = \overline{\eta} \times G \tag{7.10}$$

with

$$G \equiv \frac{Area_{top}}{Area_{PV}} \tag{7.11}$$

The gain, G, is the ratio of the LSC top area (facing the sun) to the PV area on the edges of the LSC. LSC gain is the product of the solar-averaged optical efficiency $\overline{\eta}$ and the gain, G. Hence, LSC gain is a measure of the additional number of photons collected with an LSC versus exposing the PV cell directly to the sun without an LSC.

An LSC is only meaningful when $G > 1$ since $G = \frac{Area_{PV}}{Area_{PV}} = 1$ is exactly the number of photons collected by PV cells without an LSC. Therefore, in addition to maximizing optical efficiency, we also seek to optimize LSC gain $\overline{\Gamma}$.

LSC gains increases with the side length of a square perovskite thin film LSC. This shows that perovskites are very effective at trapping light. This is due to their high refractive index, $n_{perovskite} = 2.5$, with respect to the surrounding air. Therefore, more photons are totally internally reflected and collected by the PV cells at the edges.

Chapter 8

Perovskites as Hightly Efficient LSCs

As discussed in section 6.3, Perovskite displays several properties that make them attractive for implementation as LSCs. These properties include photoluminescense, a broad absorption band, high quantum yields, high refractive index, and low-cost manufacturing techniques.

Our objective is to use our MC simulation framework of the previous section 7 to provide insight into perovskite LSCs. We aim to compare the number of absorption occurrences between perovskite and other common LSC materials, quantify optical efficiency, and optimize thickness and composition for perovskite LSCs.

Here we discuss our goals in determining the theoretical feasibility for perovskite use as an LSC by parameter and composition optimizations.

8.1 LSC Optimization Goals

Our main objective goals are to produce luminscent solar concentrators that have:

- Optimal compositions
- Limited losses due to self absorption and scattering
- Optimized dimensional designs
- Highly efficient
- Optimized by a realistic, computationally fast approach

Currently perovskite with a specified composition, thickness, and dimension is synthesized in the lab and then various properties are measured. This includes quantum yield and efficiency. Producing multiple samples and slowly varying a single parameter can be time consuming and expensive.

Furthermore, there are some properties that are not possible to measure. This is where theoretical computations provide insight into the behaviour of light inside of the device and even theoretically optimize LSC design parameters to inform which designs may produce the highest efficiencies.

8.1.1 Optimal Compositions

LSCs can be made using a variety of material compositions, each with it's own advantages and downfalls. Theoretical computations can determine which compositions display more promising potential to be an efficient LSC.

We will evaluate the effectiveness of the following compositions:

- Perovskite thin film
- Perovskite quantum dots
- CdSe-CdTe quantum dots
- Perovskite using iodide halide
- Perovskite using chloride halide
- Perovskite using partial chloride/partial acetate halide
- Perovskite using acetate halide

8.1.2 Limited losses due to self absorption and scattering

The self absorption and scattering losses are influenced by the following factors:

- Number of absorption occurrences
- Refractive index

We aim to quantify the effect of these two properties on LSC performance.

8.1.3 Optimized dimensional designs

LSCs should also have optimized designs to maximize performance. The following design parameters may be optimized:

- LSC thickness
- LSC length/width
- LSC concentration (when implementing quantum dots)

8.1.4 Highly efficient

LSCs are considered efficient when their gain, equation (7.10), is greater than 1. The higher the gain, the more efficient the LSC. Various factors that effect LSC efficiency include:

- Absorption and emission spectra
- Quantum yield
- Refractive index

8.1.5 Optimized by a realistic, computationally fast approach

Finally, optimizing various aspects of LSCs is only practical when optimized by a computationally fast approach. Furthermore, the computational approach should closely represent performance under realistic conditions. The following aspects contribute to realistic, fast computation:

- Vectorized ray tracer
- Rays selected from normalized solar spectrum
- Incorporated parameters, such as refractive index, quantum yield, dimensions

8.2 Fewer Reabsorption Occurrences Using Perovskites

Notice that there is very little overlap in the perovskite absorption and emission spectrum in Figure 7.2. Therefore, multiple absorption-emission events are less likely to occur than for other materials used as LSCs, such as Rhodamine-B. Perovskites have a smaller region of overlap between the emission and absorption spectra than either the organic dye Rhodamine-B or CdSe-CdTe quantum dots, which have previously been studied as LSCs. The absorption and emission spectra of these two materials are shown in Sahin, Ilan, and Kelley, 2011.

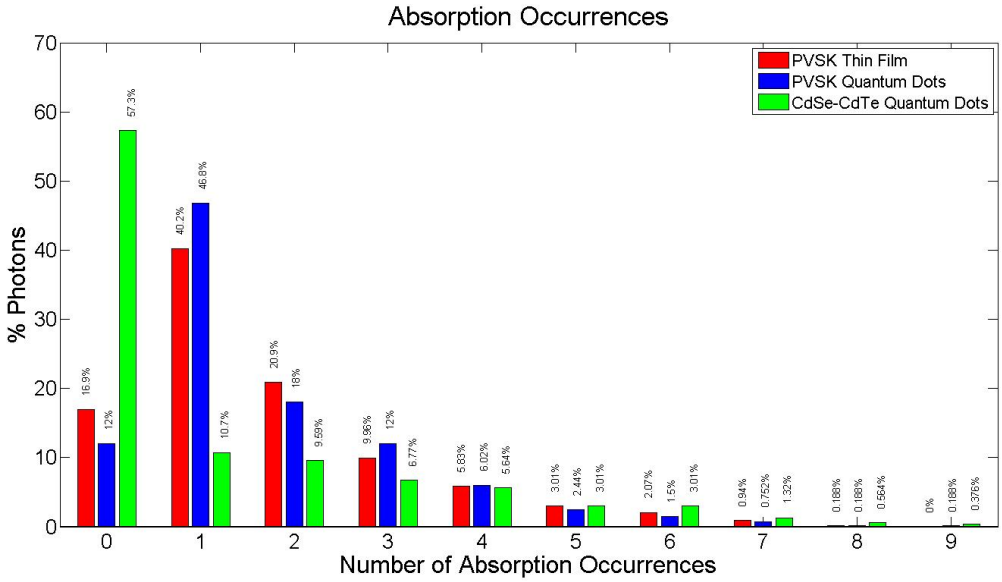

FIGURE 8.1: Comparison of the number of photon absorption occurrences in CdSE-CdTe quatum dot LSCs vs. perovskite thin film and quantum dot LSCs

Quantitatively, for a 5cm $\times$ 5cm square perovskite thin film of 800nm thickness, most photons in the perovskite LSCs are absorbed and emitted exactly once or twice, as shown in Figure 8.1. Photons undergoing absorption/emission exactly once is optimal for an LSC material since this reduces self-absorption losses. Two absorption/emissions occurrences are the second most optimal case, followed by three, and so on.

The majority of photons in CdSe-CdTe LSCs are not absorbed, as a result of its narrower absorption spectra, which means fewer photons are absorbed, specifically in the range of the highest solar radiance. In terms of absorption and emission spectra, perovskites make a more ideal LSC material than previously used organic dyes, such as CdSe-CdTe or Rhodamine-B.

8.3 Higher Percent of Collected Photons

Due to the higher number of photons absorbed by the LSC material in perovskite LSCs, a higher percent of photons are collected in perovskite LSCs versus CdSe-CdTe quantum dot LSCs as shown in Figure 8.2. This is despite the fact that perovskite LSCs display more non-radiative losses than CdSe-CdTe quantum dots since perovskites have a lower quantum yield. CdSe-CdTe quantum dot have a quantum yield of 90%, versus perovskite, which has a quantum yield around 70%.

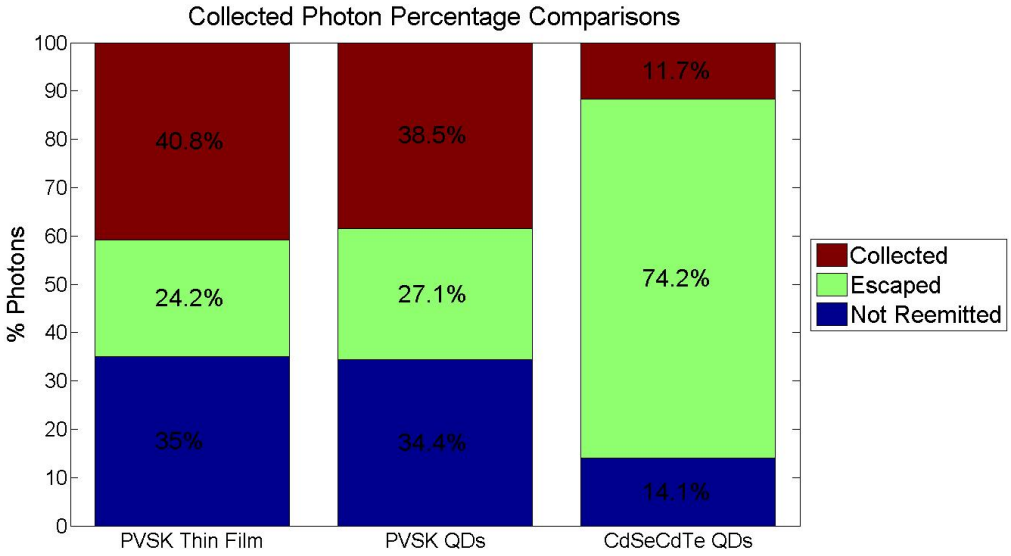

FIGURE 8.2: Comparison of photons collected, lost through the top surface, or lost due to non-radiative effects in perovskite thin film or quantum dot and CdSe-CdTe quantum dot LSCs

This lower quantum yield of perovskite is displayed by the fact that both perovskite thin film and quantum dots have more losses due to self-absorption, displayed in Figure 8.2 in blue labeled "Not Reemitted". However, the significantly higher losses due to top surfaces losses in CdSe-CdTe quantum dots make the overall percentage of collected photons much smaller than the percent collected by perovskite LSCs. The high refractive index of perovskite, along with its broader absorption spectrum decrease the amount of top surfaces losses compared to other LSC materials.

8.4 Optimal Perovskite Thickness

Gains much greater than 1 were obtained in perovskite LSCs. Gain increased with decreasing thickness. When used in an application, a lower bound on LSC thickness must be determined which is practical. Extremely thin LSCs are not practical since the power output will be negligible. Therefore, it is better to optimize the percentage of collected photons with respect to perovskite LSC thickness.

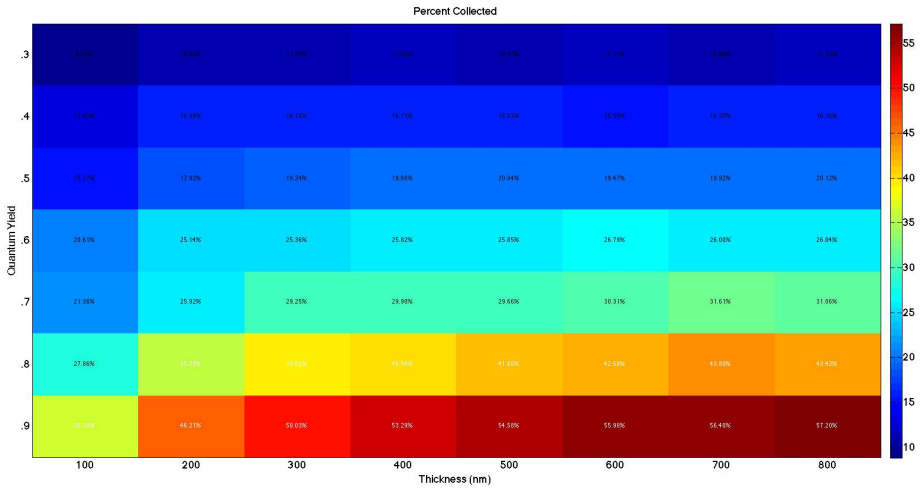

FIGURE 8.3: Collected photons for various perovskite LSC quantum yields and thicknesses.

As shown in Figure 8.3, the optimal thicknesses are in the upper-mid range around 600nm, but depend on the quantum yield. For a specified quantum yield, there is a balances between the negative effects in thin and thick LSCs films.

For example, thin films suffer from more top surface losses initially since more photons pass right through the material and are not absorbed. On the other hand, as the LSC thickness increases, photons have more material to pass through to reach the edges even with total internal reflection. This increases the chance that photons will be absorbed again by the LSC material, increasing self-absorption losses.

Our theoretical results in Figure 8.3 indicate that for a quantum yield of .6, optimum thickness is obtained around 600nm. However, as quantum yield increases to .7, an optimal thickness would increase to 700nm. This makes sense since higher quantum yields mean fewer self-absorption losses. As the quantum yield increases, the thickness can be increased to reduce top-surface losses without significantly increasing self-absorption losses.

Figure 8.4 shows that fewer photons are initially absorbed in thin LSCs, decreasing the percent of collected photons. This again displays the balance between quantum yield and LSC thickness.

Thin LSCs absorb fewer protons initially, as can be seen in Figure 8.4, but they also have much lower percentages of photons absorbed several times. This is due to the fact that thinner LSCs have less photoluminescent material between the incident photons and the PV at the edges. Furthermore, thinner LSCs are better able to serve as a wave guide, preventing photons from escaping through the top surface.

Thicker LSCs absorb more photons initially, but have more photons lost internally due to non-radiative effects. This effect is displayed in the fact that a higher percentage of photons undergo several absorption and emission events before reaching the PV.

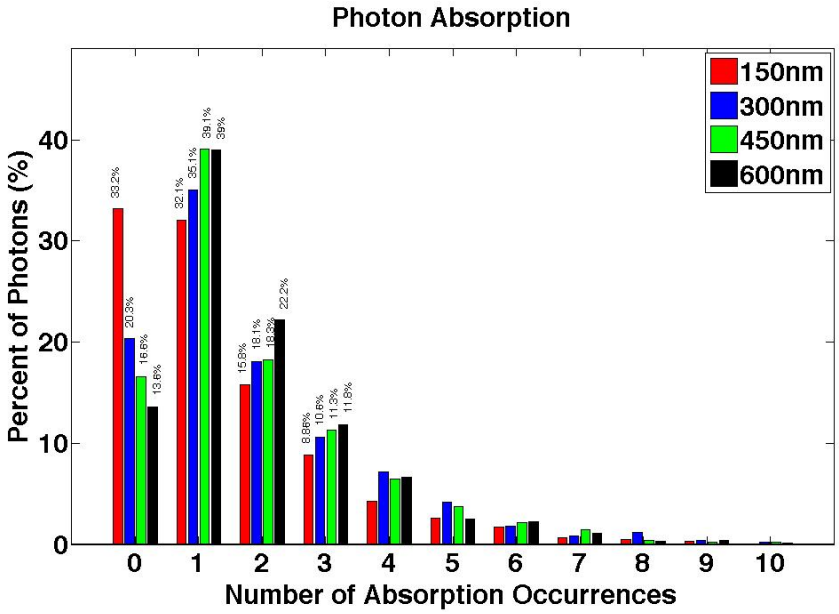

FIGURE 8.4: Absorption occurrences for perovskite LSCs of various thicknesses

8.5 Optimal Perovskite Composition

Four different compositions of perovskite were compared to determine LSC composition optimality. The halide anion was varied between 100% iodide, 100% chloride, 50% chloride with 50% acetate, and 100% acetate.

The halide composition of perovskites effects quantum yield of the material. The quantum yields of these four compositions were 38%, 52%, 83%, and 87% respectively.

As shown in Figure 8.5, increasing quantum yield resulted in an expected decrease in the amount of photons lost due to non-radiative effects. This is shown by the decreasing amount of blue “Not Reemitted" losses shown in the wedge bar chart inset moving left to right from 100% iodide to 100% acetate.

However, 100% acetate showed slightly higher top surface losses, as shown by the thicker wedge of “escaped" losses compared with other compositions. However, overall the slight increase in top surface losses was significantly outweighed by the large decrease in self-absorption losses.

The percentage of collected photons, shown by the maroon bar wedge, for 100% acetate is more than double that of 100% iodide anion. This notes a significant increase in performance using acetate anion instead of iodide or other anions for use in making perovskite LSCs.

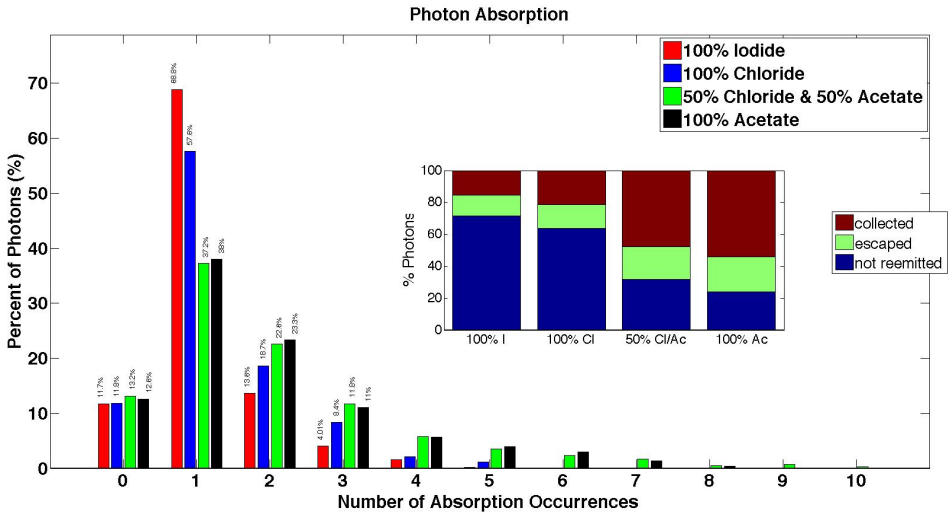

FIGURE 8.5: Comparison of the number of absorption occurrences for various halide anions

Since a high quantum yield corresponds to a higher percentage of absorbed photons that are emitted, there is a higher number of photons absorbed and emitted multiple times. The composition of 100% iodide had the highest number of photons absorbed exactly once, as shown by the bar graph in Figure 8.5.

However, 62% of those absorbed photons were lost due to non-radiative effects. Quantum yield is assumed to only effect emission, not absorbance, of the perovskite thin film. Therefore, it is determined that perovskite made with 100% acetate make the most effective LSCs.

Chapter 9

Conclusions

We presented a computationally efficient vectorized Monte Carlo simulation design for rectangular LSCs. Our theoretical results indicate that perovskite LSCs make viable, efficient LSCs. We also incorporated some improvements in speed and practicality compared to previous models that were used in LSC studies.

9.1 Achievements and Results of Method

Our computational method addressed all of our goals:

- Optimal compositions
- Limited losses due to self absorption and scattering
- Optimized dimensional designs
- Highly efficient
- Optimized by a realistic, computationally fast approach

Our MC simulation also provides flexibility in both LSC material choice, and initial top surface transmission angle. We do not require photons to enter the LSC perpendicular to the top surface, unlike previous methods.

Monte Carlo can be used to optimize LSC composition and thickness, as well as to quantitatively evaluate the effect of various loss mechanisms, such as surface losses or non-radiative effects. Theoretical Monte Carlo calculations may also be used to identify more suitable perovskite chemical compositions to be used as LSCs.

Most importantly, our theoretical results provide insight into properties that are difficult to measure, time consuming or expensive to obtain experimentally. Our theoretical Monte Carlo simulations provide insight into the number of absorption occurrences that photon undergo within an LSC. Such measurements would be difficult to obtain experimentally. Our model is also able to provide theoretical optimal values, such as LSC thickness. Optimizing thickness experimentally by creating numerous samples of varying thickness is both more expensive and time consuming than obtaining theoretical values.

9.1.1 Optimal Compositions

We investigated the following materials for use as LSCs:

- Perovskite thin films
- Perovskite quantum dots
- CdSe-CdTe quantum dots
- Perovskite using iodide halide
- Perovskite using chloride halide
- Perovskite using partial chloride/partial acetate halide
- Perovskite using acetate halide

We found that 100% acetate halide anion perovskite thin films are likely the most viable candidates for LSCs. The higher quantum yield of perovskites made with acetate makes them more ideal candidates by reducing self-absorption losses.

9.1.2 Limited losses due to self absorption and scattering

The self absorption and scattering losses are influenced by the following factors:

- Number of absorption occurrences
- Refractive index

We quantified the effect of these two properties on LSC performance. We concluded that perovskite LSCs, both thin film and quantum dot, have significantly fewer losses through the top surface as compared to CdSe-CdTe quantum dots LSCs. This is due to the broad absorption spectrum of perovskites, which absorb a large percentage of the light entering the LSC. A majority of the photons that enter CdSe-CdTe quantum dot LSCs are not even absorbed once.

As previously mentioned, the probability of emission diminishes with number of absorption-emission events due to the quantum yield. Therefore, most photons should ideally be absorbed and emitted exactly once before reaching PV. The probability of absorption depends on the overlap between adsorption and emission spectra. A much higher percentage of photons in perovskite LSCs were absorbed exactly once as compared to CdSe-CdTe quantum dots.

Fewer photons undergo a large number of absorption occurrences in perovskite LSCs. Perovskites have a lower quantum yield, which means more self-absorption losses. However, the increase in initially absorbed photons and high refractive index help significantly decrease the top surface losses. The decrease in top surface losses makes up for these increase in self-absorption losses. Overall, perovskites LSCs collect a much larger percentage of photons at the edges of the LSC, where the PV is located.

9.1.3 Optimized dimensional designs

We found that there is a balance between perovskite LSC thickness and quantum yield. For lower quantum yields, a thinner LSC is more desirable. This reduces the distance photons must travel within the LSC and therefore reduces the number of absorption occurrences. Fewer absorption occurrences are preferred when the quantum yield is lower.

On the other hand, higher quantum yields can withstand more absorption occurrences without incurring significant additional self-absorption losses. Therefore slightly thicker LSCs are preferred for higher quantum yield perovskite LSCs so that more photons are absorbed initially.

9.1.4 Highly efficient

Perovskite LSCs were shown to have theoretically high values of gain. Some characteristics that contribute to the high efficiency of perovskite LSCs include:

- Broad absorption spectrum
- Large stokes shift between absorption and emission spectra
- Little overlap in absorption and emission spectra
- Fairly high quantum yield
- High refractive index

Photons undergo fewer absorption events with perovskite LSCs than with previously used dyes, such as Rhodamine-B. This is due to decreased overlap in the absorption and emission spectra of perovskites compared to other materials. Furthermore, more photons are absorbed by perovskites due to their broad absorption spectra covering the solar spectrum as compared to CdSe-CdTe quantum dots. However, perovskites do suffer from a slightly lower quantum yield than previously studied CdSe-CdTe quantum dots.

9.1.5 Optimized by a realistic, computationally fast approach

The following aspects were incorporated into the LSC Monte Carlo simulation to provide realistic, computational fast results:

- Vectorized ray tracer
- Rays selected from normalized solar spectrum
- Incorporated parameters, such as refractive index, quantum yield, dimensions

9.2 Monte Carlo/LSC Improvements

Below we list a few of the Monte Carlo simulation improvements that we implemented compared to previously used simulations described for use in LSC studies such as that presented by Sahin, Ilan, and Kelley, 2011 in the paper “Monte-Carlo simulations of light propagation in luminescent solar concentrators based on semiconductor nanoparticles".

9.2.1 Increased Monte Carlo Efficiency and Flexibility

We implemented a vectorized Monte Carlo method, which resulted in increased computational efficiency. The vectorized ray tracer is able to successfully evaluate the performance of any given LSC with well defined parameters in a matter of seconds.

Additionally, our code only stores the essential information of each photon in its respective column of a matrix of photons. This allows the Monte Carlo steps to be performed as matrix operations on 10^5 photons or more simultaneously. Vectorized Monte Carlo simulations greatly decrease the amount of computation time compared to methods which run in a loop.

9.2.2 Flexibility

Our Monte Carlo method also does not assume that photons which fail to be absorbed within a distance of twice the LSC thickness have “escaped". This offers increased modeling flexibility. For example, the incident photons are no longer required to enter that LSC at an angle normal to the top surface. This allows photons entering at a grazing angle to be collected by the side PV cell without being absorbed by the LSC material. It also allows photons to be absorbed at at propagation distance Δs longer than twice the thickness, given that this still lies within the LSC.

Furthermore, this allows for a greater flexibility of LSC materials used within this Monte Carlo framework. For example, LSC with non-fluorescent materials such as pure glass, can be simulated since photons are not required to be absorbed and reemitted. In this way, we can simulate the number of photons reaching the PV edges of a pure glass “LSC". Pure glass “LSCs" provide insight into the number of photons that enter at grazing angles or near the LSC periphery and are collected by the PV without being absorbed or emitted by the florescent LSC material.

Pre-Normalization to Solar Spectrum

Instead of finding the optical efficiency for individual wavelengths and then normalizing these optical efficiencies to produce a solar averaged optical efficiency, our method samples photon wavelengths directly from a normalized solar spectrum. This eliminates the need to normalize over the solar spectrum after the Monte Carlo simulation is completed since the photons used in the simulation are already proportional to the solar spectrum.

9.3 Considerations

Perovskite can be used to make highly viable LSCs with parameter optimization and when the composition is chosen wisely. However, perovskite does suffer from stability issues. Perovskite needs more stability improvements before it can become commercialized for use in LSCs since perovskite currently degrades quickly. Rapidly degrading materials would not make sense economically, so device stability should reach the approximate lifetime of the PV to which it is attached. However, we did not look into these issues in depth.

Another challenge to our theoretical results was parameter precision. We were given parameter values measured in a lab which suffer from instrumental sensitivity issues. In the absorption and emission spectra data that we were given for perovskite, the absorption spectrum falls off to approximately zero within the noise levels of the measuring device.

To rectify this issue, we use a cutoff value of 780nm wavelength. After this value, we considered perovskite absorption to be zero. However, we discovered that the percentage of photons collected are sensitive to this parameter. Whether this value is zero or some relatively small positive number greatly effects the amount of self-absorption losses.

Bibliography

Administration, US Energy Information (2019). *Energy Information Administration Monthly Energy Review*. Government Printing Office, pp. 3,175.

Audet, Charles (2014). "A Survey on Direct Search Methods for Blackbox Optimization and Their Applications". In: *Mathematics Without Boundaries: Surveys in Interdisciplinary Research*, pp. 31–56.

Audet, Charles and Warren Hare (2017). *Derivative-free and blackbox optimization*. Springer.

Bortz, John and Narkis Shatz (2007). "Iterative generalized functional method of nonimaging optical design". In: *Nonimaging Optics and Efficient Illumination Systems IV*. Ed. by Roland Winston and R. John Koshel. Vol. 6670. International Society for Optics and Photonics. SPIE, pp. 84 –98.

Concerned Scientists, Union of (2017). *Barriers to Renewable Energy Technologies*.

Conn, A, Nick Gould, and Ph Toint (1997). "A globally convergent Lagrangian barrier algorithm for optimization with general inequality constraints and simple bounds". In: *Mathematics of Computation* 66.217, pp. 261–288.

Conn, Andrew R, Nicholas IM Gould, and Philippe Toint (1991). "A globally convergent augmented Lagrangian algorithm for optimization with general constraints and simple bounds". In: *SIAM Journal on Numerical Analysis* 28.2, pp. 545–572.

Conn, Andrew R, Katya Scheinberg, and Luis N Vicente (2009). *Introduction to derivative-free optimization*. Vol. 8. Siam.

Coropceanu, Igor and Moungi G Bawendi (2014). "Core/shell quantum dot based luminescent solar concentrators with reduced reabsorption and enhanced efficiency". In: *Nano letters* 14.7, pp. 4097–4101.

Debije, Michael G and Paul PC Verbunt (2012). "Thirty years of luminescent solar concentrator research: solar energy for the built environment". In: *Advanced Energy Materials* 2.1, pp. 12–35.

Duffie, J.A. and W.A. Beckman (2013). *Solar Engineering of Thermal Processes*. Ingenieria de la Energia. Wiley.

Emery, Keith (2000). *Reference Solar Spectral Irradiance, Technical Report, ASTM*.

Gimenez-Benitez, Pablo et al. (2004). "Simultaneous multiple surface optical design method in three dimensions". In: *Optical Engineering* 43.7, pp. 1489–1503.

Golovin, Daniel et al. (2017). "Google vizier: A service for black-box optimization". In: *Proceedings of the 23rd ACM SIGKDD international conference on knowledge discovery and data mining*, pp. 1487–1495.

Green, Martin A, Anita Ho-Baillie, and Henry J Snaith (2014). "The emergence of perovskite solar cells". In: *Nature photonics* 8.7, pp. 506–514.

Hinterberger, H and R Winston (1966). "Efficient light coupler for threshold Čerenkov counters". In: *Review of Scientific Instruments* 37.8, pp. 1094–1095.

Honsberg, CB and SG Bowden (2019). *Photovoltaics education website*.

Hooke, Robert and Terry A Jeeves (1961). ""Direct Search"Solution of Numerical and Statistical Problems". In: *Journal of the ACM (JACM)* 8.2, pp. 212–229.

IRENA, IREA (2018). "Renewable power generation costs in 2017". In: *Report, International Renewable Energy Agency, Abu Dhabi*.

Jacques, Steven L and Lihong Wang (1995). "Monte Carlo modeling of light transport in tissues". In: *Optical-thermal response of laser-irradiated tissue*. Springer, pp. 73–100.

Jafrancesco, David et al. (2012). "Simple methods to approximate CPC shape to preserve collection efficiency". In: *International Journal of Photoenergy* 2012.

Kolda, Tamara G, Robert Michael Lewis, Virginia Torczon, et al. (2006). "A generating set direct search augmented Lagrangian algorithm for optimization with a combination of general and linear constraints". In: *Sandia National Laboratories* 6.

Koshel, R John (2012). *Illumination engineering: design with nonimaging optics*. John Wiley & Sons.

Koziel, Slawomir and Xin-She Yang (2011). *Computational optimization, methods and algorithms*. Vol. 356. Springer.

Laube, Philipp (2019). *Semiconductor Technology from A to Z*.

Leijtens, Tomas et al. (2015). "Stability of metal halide perovskite solar cells". In: *Advanced Energy Materials* 5.20, p. 1500963.

Lewis, Robert Michael (1996). *Rank ordering and positive bases in pattern search algorithms*. 96. Institute for Computer Applications in Science and Engineering, NASA Langley ...

Marston, AJ, KJ Daun, and MR Collins (2010). "Geometric optimization of concentrating solar collectors using monte carlo simulation". In: *Journal of solar energy engineering* 132.4.

Meinardi, Francesco et al. (2015). "Highly efficient large-area colourless luminescent solar concentrators using heavy-metal-free colloidal quantum dots". In: *Nature nanotechnology* 10.10, pp. 878–885.

Mendewala, Benaz et al. (2019). "The potential of scalability in high efficiency hybrid perovskite thin film luminescent solar concentrators". In: *Solar Energy* 183, pp. 392–397.

Miñano, Juan C et al. (2009). "Overview of the SMS design method applied to imaging optics". In: *Novel Optical Systems Design and Optimization XII*. Vol. 7429. International Society for Optics and Photonics, p. 74290C.

Nikolaidou, Katerina et al. (2016). "Hybrid Perovskite Thin Films as Highly Efficient Luminescent Solar Concentrators". In: *Advanced Optical Materials* 4.12, pp. 2126–2132.

Nocedal, Jorge and Stephen J. Wright (2006). *Numerical Optimization*. second. New York, NY, USA: Springer.

NREL, NREL (2019). *Best research-cell efficiencies*.

O'Gallagher, Joseph J (2008). "Nonimaging optics in solar energy". In: *Synthesis Lectures on Energy and the Environment: Technology, Science, and Society* 2.1, pp. 1–120.

Park, Nam-Gyu (2015). "Perovskite solar cells: an emerging photovoltaic technology". In: *Materials today* 18.2, pp. 65–72.

Rabl, Ari (1976). "Solar concentrators with maximal concentration for cylindrical absorbers". In: *Appl. Opt.* 15.7, pp. 1871–1873.

Reinhold, Arnold (2016). *Graph of California hourly electric load vs. load less solar and wind (Duck curve) for October 22, 2016 Data: California ISO - Renewables Reporting.*

Rooij, Dricus de (2019). *Luminescent Solar Concentrator Cells.*

Sahin, Derya, Boaz Ilan, and David F. Kelley (2011). "Monte-Carlo simulations of light propagation in luminescent solar concentrators based on semiconductor nanoparticles". In: *Journal of Applied Physics* 110.3, p. 033108.

Shatz, Narkis et al. (2008). "Advanced optics for LED flashlights". In: *Nonimaging Optics and Efficient Illumination Systems V*. Vol. 7059. International Society for Optics and Photonics, p. 70590D.

Sholin, V, JD Olson, and SA Carter (2007). "Semiconducting polymers and quantum dots in luminescent solar concentrators for solar energy harvesting". In: *Journal of applied physics* 101.12, p. 123114.

Stine, William and Michael Geyer (2001). "Power From The Sun by William B. Stine and Michael Geyer". In:

Torczon, Virginia (1997). "On the convergence of pattern search algorithms". In: *SIAM Journal on optimization* 7.1, pp. 1–25.

Van Sark, Wilfried GJHM et al. (2008). "Luminescent Solar Concentrators-A review of recent results". In: *Optics express* 16.26, pp. 21773–21792.

Weber, WH and John Lambe (1976). "Luminescent greenhouse collector for solar radiation". In: *Applied optics* 15.10, pp. 2299–2300.

Winston, R. et al. (2005). *Nonimaging Optics*. Electronics & Electrical. Elsevier Science.

Winston, Roland, Lun Jiang, and Melissa Ricketts (2018). "Nonimaging optics: a tutorial". In: *Adv. Opt. Photon.* 10.2, pp. 484–511.

Works, Math (2020a). *Pattern Search Options.*

— (2020b). *Set Options Pattern Search.*

Yang, Jinli et al. (2015). "Investigation of $CH_3NH_3PbI_3$ degradation rates and mechanisms in controlled humidity environments using in situ techniques". In: *ACS nano* 9.2, pp. 1955–1963.